

General 3-D Steady-State Analysis of Travelling Halbach Rotor Above a Conductive Plate

Cai Yundi Elliot

03 December 2025

Abstract

This research presents a comprehensive three-dimensional steady-state analysis of a travelling Halbach rotor operating above a conductive plate. The study aims to derive analytical expressions that describe the interaction between the rotor's time-varying magnetic field and the induced eddy currents in a nearby conductive medium. In the first approach, a 3-D magnetic charge model is utilized to find the exact magnetic scalar potential, force production, and flow of eddy currents under a thin-sheet approximation. In the second, a Poisson–Laplace analysis is carried out—including separation of variables, Bessel functions, and the use of an orthogonal greedy algorithm—to simplify the complex expressions by a hybrid numerical and analytical model.

The research derives the magnetic scalar potential as an infinite series and associated magnetic field components using Fourier–Laplace techniques. These analytical developments are validated against finite element method (FEM) simulations, ensuring efficient simulation times and accurate modelling. The study shows that the induced eddy currents generate both levitation and drag forces, which can be utilized in applications like maglev transportation [8], dampers [24], eddy current brakes [29, 26], and electric vehicles [18].

Keywords: Halbach rotor, 3-D magnetic charge model, steady-state analysis, magnetic scalar potential, finite element method

Contents

1	Introduction	3
2	A Brief Introduction to the Halbach Rotor	3
2.1	Structural Parameters and Equations	4
3	Green's Function Approach - Magnetic Charge Model	6
3.1	Model Assumptions and Basic Parameters	6
3.2	Magnetic Components	7
3.3	Magnetic Charge Model with Conductive Plate	10
3.3.1	Correlation of Eddy Current and Wave Equation	10
3.3.2	Propagation of the Image Magnetic Charge	11
3.4	Model Evaluation	16
4	3-D Laplace-Poisson Approach – Magnetic Scalar Potential Model	17
4.1	Governing Parameters and Equations	17
4.1.1	Region Definition	17
4.1.2	Parameter Address	17
4.2	Boundary Conditions	18
4.3	General Form of the Source Field	18
4.4	Solving with Hybrid Analytical-Numerical Method	19
4.4.1	Failing of Pure Analytic Model	19
4.4.2	Orthogonal Greedy Algorithm	20
4.5	Implementation and Results of the Hybrid Analytical-Numerical Method	21
4.6	Overall Evaluation	22
4.6.1	Advantages Over Pure Analytical and Numerical Model	22
4.6.2	Future Works	22
5	Governing Equations for Magnetic Source on Conductive Plate	23
5.1	Conductive Plate Region	23
5.2	Non-conductive Region	24
5.3	Boundary Conditions	24
6	Fourier Analysis on Problem Region	26
6.1	Transformed Governing Equations	26
6.2	Transformed Boundary Equations	26
6.3	Gauge Transformation	27
6.4	Magnetic Force	28
6.5	Power Loss	29
7	Numerical Approximation by Finite Element Method	30
7.1	Weak Form Formulation	30
7.2	Upwinding	31
7.3	Result Plot	32
8	Model Comparison	34
8.1	Source Field Comparison	34
8.2	Plate Components Comparison	34
9	Conclusion	35
9.1	Research Result	35
9.2	Future Analysis	35
A1	Green's Function for the Laplace Operator	38

A2	Integral Transformation of Derivative Functions	40
A3	Details and Results of Orthogonal Greedy Algorithm	41
A4	Coefficients of Magnetic Components in the Air and Plate Region	51

1 Introduction

When a magnetic source moves or rotates above a conductive plate, it generates a time-varying magnetic field that induces eddy currents, as described by Maxwell's equations. These induced currents create a magnetic field that interacts with the magnetic source, producing both normal and tangential forces. The normal force is responsible for the levitation effect, while the tangential force generates a drag on the rotor, dissipating excess energy. The non-contact nature of the force production makes it suitable for various applications such as maglev transportation [8], dampers [24], eddy current brakes [29, 26], and electric vehicles [18].

Some studies take a 2-D approach and solve the steady-state equations approximately by the thin-sheet approximation [19?] or exactly by Fourier–Laplace transform [22]. A few have derived equations for a 3-D model, but their solutions rely on finite element methods [7, 32], which can result in lengthy simulation times during the development of advanced control strategies when coupling the numerical software with simulation software. In this paper, we aim to provide a clearer understanding of the steady-state equations of the Halbach rotor on a conductive plane by adapting multiple 3-D models to describe the magnetic field and forces acting on both the source and the conductive plate.

2 A Brief Introduction to the Halbach Rotor

A Halbach rotor is a commonly used mechanical instrument created by specialized arrays of permanent magnets. The magnets are arranged in a specific pattern to reinforce the magnetic field on one side while weakening it on the opposite side. This creates a sinusoidal magnetic field distribution, which reduces cogging torque and facilitates smooth operation. This property makes it ideal for applications requiring high-efficiency magnetic coupling, such as energy harvesting and eddy-current-based devices [4].

In general, there are two types of polarities: radial charge polarity and azimuthal charge polarity.



Figure 1: Demonstration of the radial charged polarity and azimuthal charged polarity taken from [7].

When two oppositely polarized, radially charged permanent magnets are put together, they create a magnetic field that follows their direction of magnetization. On the other hand, azimuthally charged permanent magnets create a magnetic field from the tip to the end of the magnetisation direction outside the permanent magnet. When they are arranged together, the magnetic field on the side of the arranged magnets is enhanced, while the other side is reduced.

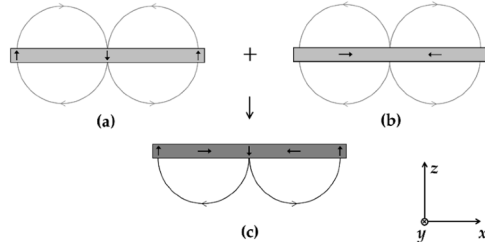


Figure 2: Illustration of the enhancing and cancelling effects adapted from [25].

This property stretches the magnetic lines on a particular side and creates a strong self-shielding effect, which generates an ideal sinusoidal magnetic source field. It increases the power density compared to the classical configuration [11].

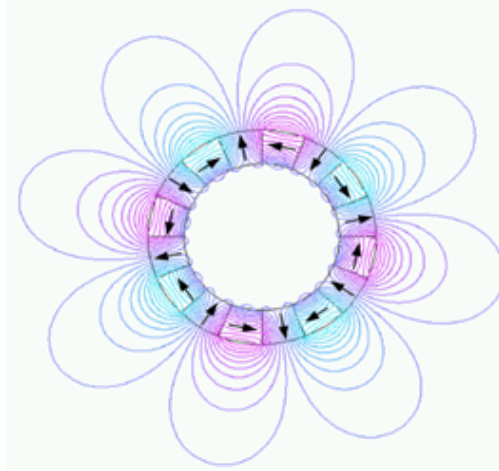


Figure 3: A 2D demonstration of the magnetic field of a 4-pole pair external Halbach rotor (external strong field) taken from [2].

The strong power density and self-shielding effect allow the Halbach rotor to use non-core materials (other than magnetic materials) in classical configurations. The wide range of material selection can reduce the rotational inertia effectively, which eventually leads to a reduction in redundant power dissipation.

In automotive applications, Halbach rotors typically use high-coercivity NdFeB magnets for optimal thermal stability and energy density. Bonded NdFeB (e.g., Magfine MF18P) is ideal for Halbach arrays due to:

- Manufacturing flexibility: Injection moulding enables precise anisotropic magnetization for ideal field distribution.
- High electrical resistivity ($120 \mu\Omega \text{ m}$ – $150 \mu\Omega \text{ m}$): Eddy current losses are reduced by more than a hundredfold compared to sintered magnets.
- Recyclability: Disassembly and reuse of magnet powder are simplified (up to 30% recycled content without performance loss).

The sinusoidal flux profile allows pairing with fractional-slot concentrated windings, further improving torque density and fault tolerance in EV/HEV motors. These properties make this specific arrangement of magnets widely used in different industries.

2.1 Structural Parameters and Equations

The following properties and assumptions are captured in the constructed equations:

- The permanent magnet is current-free [31].
- The magnetization remains constant despite the external magnetic field due to the high coercivity of the permanent magnet.
- The magnets are arranged in a periodic pattern, with the magnetisation being continuous and its angle to the vertical proportional to θ/P .
- The magnet is ideal and identical, such that it is fully magnetised in the direction of magnetisation.
- Flux leakage and air gaps are neglected.
- The permittivity in the air space is constant.
- The conductive plate is large enough that the magnetic field components vanish at its edges (Dirichlet boundary condition).

The magnetisation is defined as:

$$\vec{M} = M_0 \left[\cos(P\theta) \hat{\rho} \mp \sin(P\theta) \hat{\theta} \right] \quad (1)$$

where M_0 represents the magnitude of magnetization. The negative sign indicates an external rotor machine, where the strong magnetic field is located outside and the weak field is inside the rotor, and vice versa.

Table 1: Parameters for Halbach Rotor Analysis

Parameter	Definition	Value
R_i	Inner radius	0.005 m
R_o	Outer radius	0.015 m
W_r	Width	0.02 m
M_0	Magnetization of NdFeB [9]	$1 \times 10^6 \text{ A m}^{-1}$
P	Pole pairs	4
h_r	Height of the rotor above the conductive plate	0.02 m
d_p	Thickness of the conductive plate	0.005 m
v_x	Velocity of the rotor along the x-axis	0.05 m s^{-1}
ω_m	Angular velocity of the rotor	5 rad s^{-1}
σ	Conductivity of plate	$3.8 \times 10^7 \text{ S m}^{-1}$

These parameters are consistent throughout the report in the numerical analysis.

3 Green's Function Approach - Magnetic Charge Model

A review of the relevant literature reveals that deriving a simple equation to characterize the magnetic field and the forces generated by eddy currents in a Halbach rotor is quite difficult. This complexity stems from the necessity of multiple infinite series, often involving Bessel functions and Fourier series, which complicates analytical solutions [20].

In this section, we present an exact solution for the magnetic field using a magnetic charge model. By making assumptions such as the thin sheet approximation and adjusting our approach to modeling the rotor movement, we simplify the problem. These simplifications lead to a general and relatively straightforward approximation equation that effectively captures the key physical interactions involved.

The table below shows the values of the parameters modified or added for evaluating numerical results.

Table 2: Modified Parameters for Magnetic Charge Model

Parameter	Definition	Value
v_p	Velocity of the image magnetic charge	5000 m s^{-1}
d_p	Thickness of the conductive plate	$\approx 0 \text{ m}$

3.1 Model Assumptions and Basic Parameters

The following assumptions are made:

- The width of the conductive plate is significantly smaller than both the height and the dimensions of the rotor.

The magnetic volume charge density and the magnetic surface charge density can be found in Furlani (2001):

$$\rho_m = -\vec{\nabla} \cdot \vec{M} = -M_0 \frac{1}{\rho} \cos(P\theta)(1 \mp P) \quad (2)$$

$$\sigma_m = \vec{M} \cdot \hat{n} = \begin{cases} -M_0 \cos(P\theta), & \text{for } \rho = R_i \\ M_0 \cos(P\theta), & \text{for } \rho = R_o \\ 0, & \text{for } z = \pm W_r/2 \end{cases} \quad (3)$$

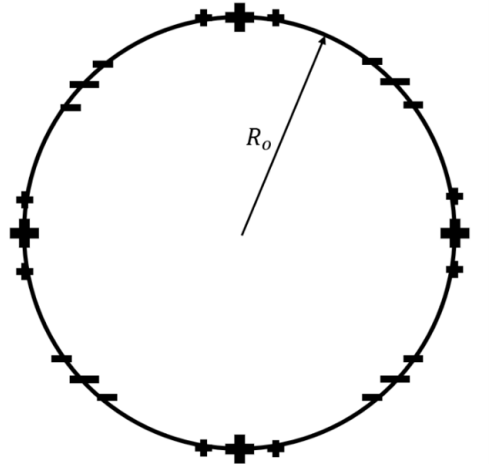


Figure 4: Illustration of the surface charge distribution of a 4-pole pair Halbach rotor

The magnetic field is given by:

$$\vec{B} = \mu_0(\vec{H} + \vec{M}) \quad (4)$$

By taking divergence on both sides, the magnetic field drops out because of the Maxwell equation $\vec{\nabla} \cdot \vec{B} = 0$. By substituting the magnetic scalar potential ϕ into the equation, the following is obtained:

$$\vec{\nabla} \cdot \vec{M} = \nabla^2 \phi_m \quad (5)$$

The Green's function for the Laplace operator is given by (detailed derivation provided in Appendix 1):

$$g(\vec{x}, \vec{x}') = \frac{1}{4\pi|\vec{x} - \vec{x}'|} \quad (6)$$

The magnetic scalar potential can be found by:

$$\begin{aligned} L[g] &= -\delta(x - x') \\ L[g] \vec{\nabla}' \cdot \vec{M}' &= -\delta(x - x') \vec{\nabla}' \cdot \vec{M}' \\ \iiint_{\tau'} L[g] \vec{\nabla}' \cdot \vec{M}' d\tau' &= - \iiint_{\tau'} \delta(x - x') \vec{\nabla}' \cdot \vec{M}' d\tau' \\ -\frac{1}{4\pi} \iiint_{\tau'} \frac{\vec{\nabla}' \cdot \vec{M}'}{|\vec{x} - \vec{x}'|} d\tau' &= L^{-1}[\vec{\nabla} \cdot \vec{M}] \\ \phi_m &= \frac{1}{4\pi} \left(\iiint_{\tau'} \frac{\rho'_m}{|\vec{x} - \vec{x}'|} d\tau' + \iint_{a'} \frac{\sigma'_m}{|\vec{x} - \vec{x}'|} da' \right) \end{aligned} \quad (7)$$

Here, the prime denotes the source point, and $L = \nabla^2$ is the Sturm-Liouville operator or the Laplace operator.

3.2 Magnetic Components

Using this model, both the magnetic scalar potential and the magnetic field can be computed at a point (ρ, θ, z) .

To better capture the behaviour, the quantity φ is introduced, accounting for the initial angle shift:

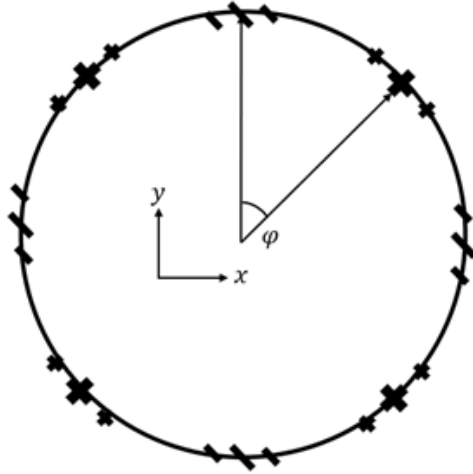


Figure 5: Illustration of the angle shift

The magnetic scalar potential can be computed by equation (7), which can be rewritten as:

$$\phi_m(\rho, \theta, z) = \frac{M_0}{4\pi} \begin{cases} - \int_{-W_r/2}^{W_r/2} \int_{\theta}^{2\pi+\theta} \int_{R_i}^{R_o} \frac{\cos^{P(\theta'-\varphi)}(1 \mp P)}{\sqrt{\rho^2 + \rho'^2 - 2\rho\rho' \cos(\theta-\theta') + (z-z')^2}} d\rho' d\theta' dz' \\ - \int_{-W_r/2}^{W_r/2} \int_{\theta}^{2\pi+\theta} \frac{\cos[P(\theta'-\varphi)]}{\sqrt{\rho^2 + R_i^2 - 2\rho R_i \cos(\theta-\theta') + (z-z')^2}} R_i d\theta' dz' \\ + \int_{-W_r/2}^{W_r/2} \int_{\theta}^{2\pi+\theta} \frac{\cos[P(\theta'-\varphi)]}{\sqrt{\rho^2 + R_o^2 - 2\rho R_o \cos(\theta-\theta') + (z-z')^2}} R_o d\theta' dz' \end{cases} \quad (8)$$

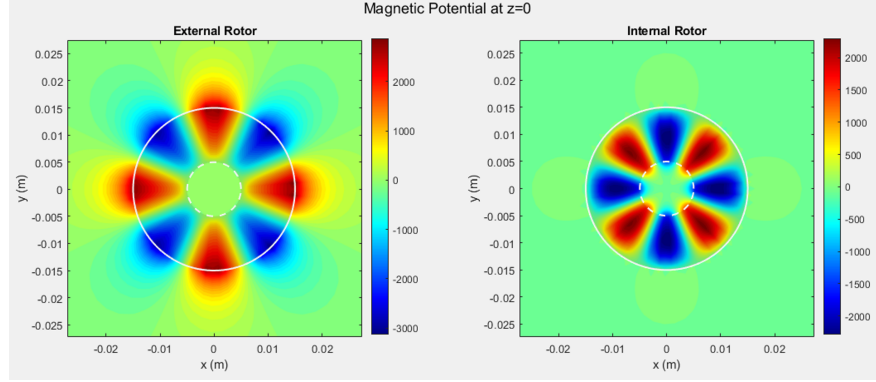


Figure 6: Graph of the magnetic scalar potential on $z = 0$ for the external and internal rotor, respectively (the white line and dotted line indicate the outer and inner radius of the rotor)

A periodic behaviour of the magnetic scalar potential is observed with a period of $2\pi/P$.

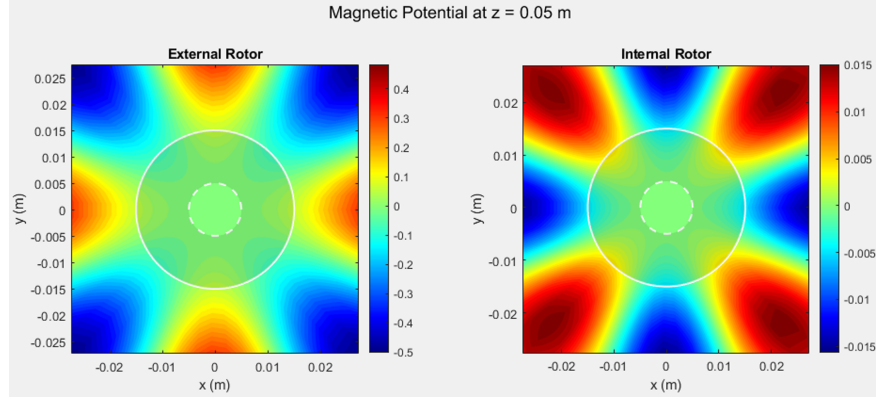


Figure 7: Value of magnetic scalar potential for $z = 0.05\text{m}$ for the external and internal rotor, respectively

When the value of z increases, the field is more dispersed, while the field magnitude decreases significantly. The 3D plot illustrates the decaying nature of the magnetic scalar potential of the rotor.

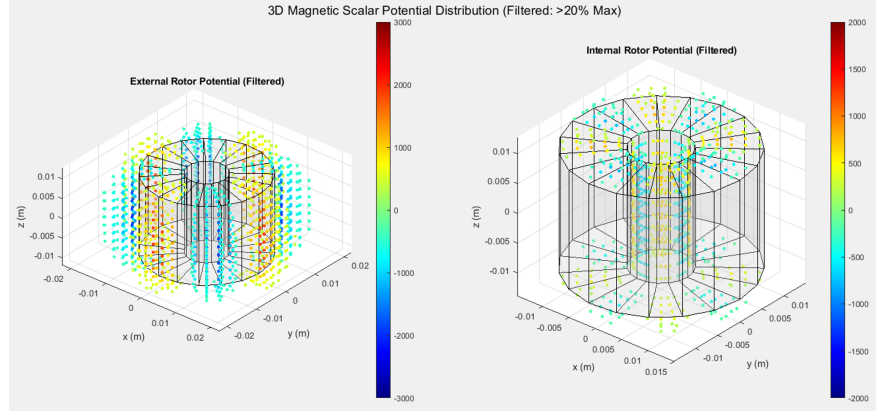


Figure 8: Graph of 3D magnetic scalar potential for the external and internal rotor, respectively (values lower than 20% are not plotted)

The magnetic field strength is related to the magnetic scalar potential by:

$$\vec{H} = -\vec{\nabla}\phi = -\frac{\partial\phi_m}{\partial\rho}\hat{\rho} - \frac{1}{\rho}\frac{\partial\phi_m}{\partial\theta}\hat{\theta} - \frac{\partial\phi_m}{\partial z}\hat{z} \quad (9)$$

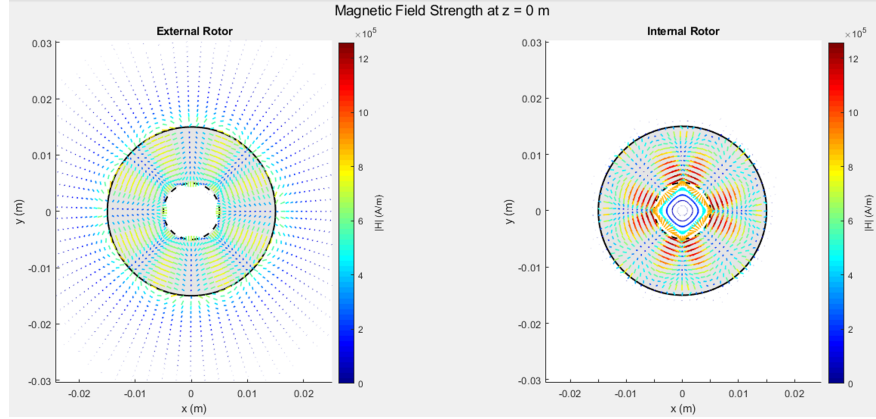


Figure 9: Magnitude and direction of magnetic field strength for $z = 0$ for the internal and external rotor, respectively

The magnetic field in all regions can be computed by:

$$\vec{B} = \begin{cases} \mu_0 \left[- \left(\frac{\partial\phi_m}{\partial\rho}\hat{\rho} + \frac{1}{\rho}\frac{\partial\phi_m}{\partial\theta}\hat{\theta} + \frac{\partial\phi_m}{\partial z}\hat{z} \right) + M_0 \left[\cos(P\theta)\hat{\rho} \mp \sin(P\theta)\hat{\theta} \right] \right], \\ \text{for } (\rho, \theta, z) \in R_i < \rho < R_o \text{ and } |z| < W_r/2 \\ -\mu_0 \left(\frac{\partial\phi_m}{\partial\rho}\hat{\rho} + \frac{1}{\rho}\frac{\partial\phi_m}{\partial\theta}\hat{\theta} + \frac{\partial\phi_m}{\partial z}\hat{z} \right), \quad \text{otherwise} \end{cases} \quad (10)$$

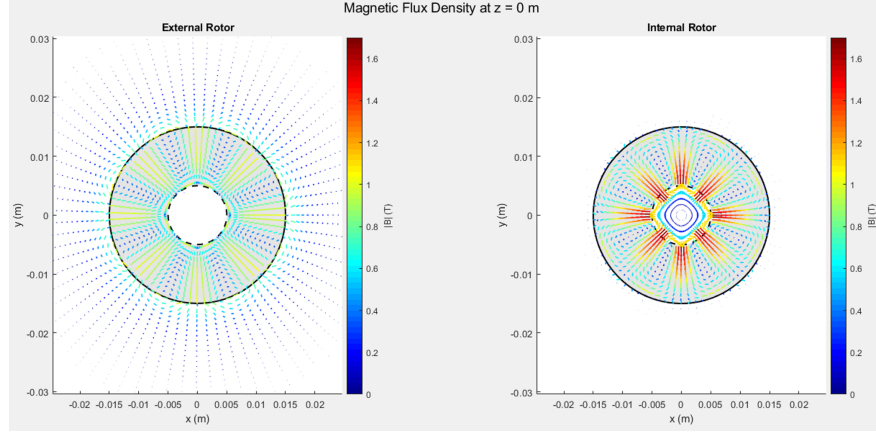


Figure 10: Magnitude and direction of the magnetic field strength for $z = 0$ for the internal and external rotor, respectively

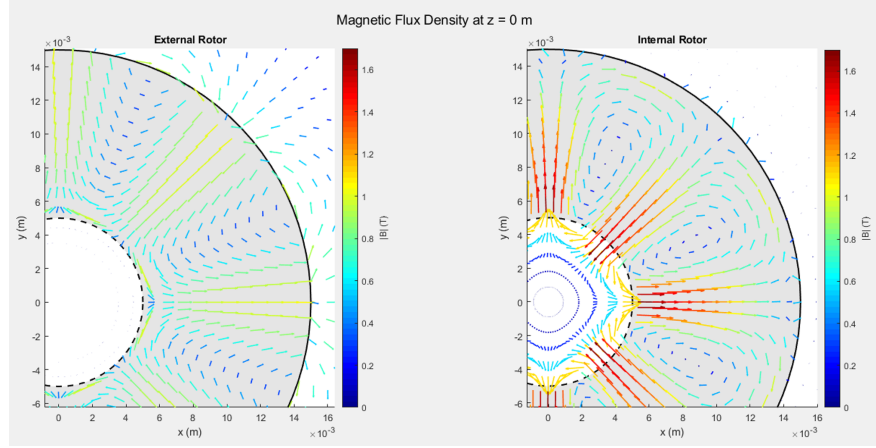


Figure 11: Magnitude and direction of the magnetic field strength for $z = 0$ for the internal and external rotor, respectively

3.3 Magnetic Charge Model with Conductive Plate

3.3.1 Correlation of Eddy Current and Wave Equation

In this section, the relationship between induced eddy currents and the wave equation is explored by utilizing the thin sheet approximation. We aim to simplify the complex interactions between electromagnetic fields and conductive materials.

The Maxwell equation gives:

$$\vec{\nabla} \times \vec{E} = -\frac{\partial \vec{B}}{\partial t} \quad (11)$$

$$\vec{\nabla} \times \vec{B} = \mu_0 \vec{J} + \mu_0 \epsilon_0 \frac{\partial \vec{E}}{\partial t} \quad (12)$$

Neglecting the displacement current and utilizing the fact that $\vec{J} = \sigma \vec{E}$,

$$\nabla^2 \vec{B} = \mu_0 \sigma \frac{\partial \vec{B}}{\partial t} \quad (13)$$

As $d_p \ll h_r$, the equation reduces to:

$$\frac{\partial^2 B_y}{\partial y^2} = \mu_0 \sigma \frac{\partial B_y}{\partial t} \quad (14)$$

Where d_p and h_r are the thickness of the plate and the height of the rotor, respectively.

Since d_p is small, the equation can be expressed as a first-degree derivative for the region $y \approx 0$ given by:

$$\frac{\frac{\partial B_y}{\partial y} \Big|_y - \frac{\partial B_y}{\partial y} \Big|_{-y-d}}{2y + d_p} = \mu_0 \sigma \frac{\partial B_y}{\partial t} \quad (15)$$

Since the region across is small, $\partial B_y / \partial y$ can be treated as an odd function for $y \approx 0$. Therefore,

$$\frac{\partial B_y}{\partial y} = \frac{\mu_0 \sigma d_p}{2} \frac{\partial B_y}{\partial t} \quad (16)$$

For a typical wave equation,

$$\left[\left(\frac{1}{v} \frac{\partial}{\partial t} - \frac{\partial}{\partial y} \right) \left(\frac{1}{v} \frac{\partial}{\partial t} + \frac{\partial}{\partial y} \right) \right] u = 0 \quad (17)$$

The equation derived above has the form of the half-wave equation, where the 'wave' is propagating in the negative y direction. As the magnetic charge has been related to the wave, this indicates that the image magnetic charge is propagating through the negative y direction with a speed of:

$$v_\rho = \frac{2}{\mu_0 \sigma d_p} \quad (18)$$

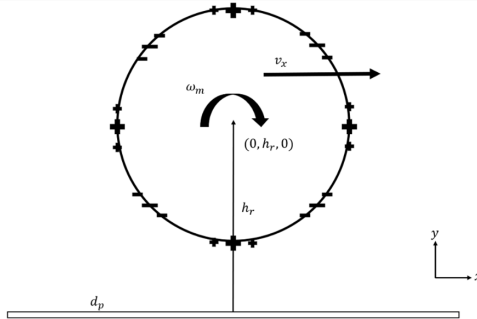


Figure 12: Visualization of the defined parameters

3.3.2 Propagation of the Image Magnetic Charge

When a conductive plate of width d_p is positioned above the plane $y = 0$, the magnetic field at $y = 0$ must be zero. Consequently, the image magnetic charge can be modelled with the same sign as the actual magnetic charge, with the position reflected along the x -axis [17].

The concept of the propagating image charge can also be extended to apply to the magnetic field in the region where $z \geq 0$. This extension is valid under the condition that the time evolution of the system is sufficiently slow relative to the response time of the conducting thin plate, i.e., the conductive plate responds instantly to the motion of the Halbach rotor [3].

The motion of the magnetic charge up to the present moment $t = 0$ is considered, with the focus on the magnetic scalar potential generated by all image charges that arise from the movement of this charge along its trajectory.

To analyse this, the magnetic charge's trajectory is broken into discrete time steps represented by an infinitesimal interval τ . The motion of the magnetic charge is modelled as a series of hops occurring at the

beginning of each time step. Each hop is characterized by the simultaneous removal of one magnetic charge and the creation of another charge, which appears at the trajectory position corresponding to the start of the current time step, while the removed charge is positioned at its trajectory location from the previous time step. However, since the image charge is propagating downward, the created counter charge cannot fully eliminate the effect of the original image charge. Instead, they are separated by a distance of $v_\rho\tau$.

By taking an infinite number of steps with an infinitesimal time interval τ , the individual hops of the magnetic charge become so small that we can effectively treat its motion as continuous. By integrating these contributions over the entire trajectory of the magnetic charge, a governing steady-state equation that accounts for both the motion of the magnetic charge and the response of the conductive plate can be derived, which describes the drag and levitating force experienced by the Halbach rotor as it moves through the conducting thin plate.

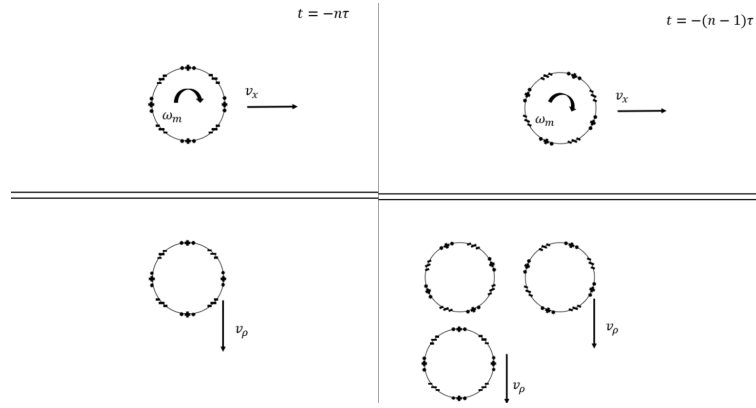


Figure 13: Illustration of the propagating image magnetic charge at time $-n\tau$ (start) and $-(n-1)\tau$ (first infinitesimal step)

By assuming that the rotor moves at a constant velocity v_x and angular velocity ω_m , the influence of the angular velocity on the charge distribution can be modelled by:

$$\rho_m(t, \theta') = \rho_{m0} \cos[P(\theta' + \omega_m t - \varphi)] \quad (19)$$

Where φ accounts for the angle shift at $t = 0$.

The current image charge, the image charge backtracking the first infinitesimal step, and the first counter image charge, denoted by ρ_0 , ρ_1 and ρ'_1 respectively, are given by:

$$\rho_0 = \rho_m(t = 0, \theta')(\rho' \sin \theta', -h_r - \rho' \cos \theta', z') \quad (20)$$

$$\rho_1 = \rho_m(t = -\tau, \theta')(\rho' \sin \theta' - v_x \tau, -h_r - \rho' \cos \theta' - v_\rho \tau, z') \quad (21)$$

$$\rho'_1 = -\rho_m(t = 0, \theta')(\rho' \sin \theta' - v_x \tau, -h_r - \rho' \cos \theta', z') \quad (22)$$

In general, the n th charge and counter charge are located at:

$$\rho_k = \rho_m(t = -k\tau, \theta'), (\rho' \sin \theta' - kv_x \tau, -h_r - \rho' \cos \theta' - kv_\rho \tau, z') \quad \forall k \in [0, n] \quad (23)$$

$$\rho'_k = -\rho_m(t = -(k-1)\tau, \theta'), (\rho' \sin \theta' - kv_x \tau, -h_r - \rho' \cos \theta' - (k-1)v_\rho \tau, z') \quad \forall k \in [1, n] \quad (24)$$

By aggregating all the contributions and setting the number of steps to infinity, which gives the steady state of the system, the total magnetic scalar potential at the point $(x, y + h_r, z)$ from all the propagating

image charges can be expressed as an infinite sum below:

$$\begin{aligned}
& - \frac{1}{4\pi} \sum_{n=0}^{\infty} \int_{-W_r/2}^{W_r/2} \int_{R_i}^{R_o} \int_{\arctan\left(\frac{x+v_x n \tau}{y+h_r + v_\rho n \tau}\right)}^{2\pi + \arctan\left(\frac{x+v_x n \tau}{y+h_r + v_\rho n \tau}\right)} \\
& \quad \frac{M_0 \cos^{P(\theta' + \omega_m n \tau - \varphi)}(1 - P)}{\sqrt{(x - \rho' \sin \theta' + v_x n \tau)^2 + (y + h_r + \rho' \cos \theta' + v_\rho n \tau)^2 + (z - z')^2}} d\rho' d\theta' dz' \\
& + \frac{1}{4\pi} \sum_{n=0}^{\infty} \int_{-W_r/2}^{W_r/2} \int_{R_i}^{R_o} \int_{\arctan\left(\frac{x+v_x(n+1)\tau}{y+h_r + v_\rho n \tau}\right)}^{2\pi + \arctan\left(\frac{x+v_x(n+1)\tau}{y+h_r + v_\rho n \tau}\right)} \\
& \quad \frac{M_0 \cos^{P(\theta' + \omega_m n \tau - \varphi)}(1 - P)}{\sqrt{(x - \rho' \sin \theta' + v_x(n+1)\tau)^2 + (y + h_r + \rho' \cos \theta' + v_\rho n \tau)^2 + (z - z')^2}} d\rho' d\theta' dz' \\
& - \frac{1}{4\pi} \sum_{n=0}^{\infty} \int_{-W_r/2}^{W_r/2} \int_{\arctan\left(\frac{x+v_x n \tau}{y+h_r + v_\rho n \tau}\right)}^{2\pi + \arctan\left(\frac{x+v_x n \tau}{y+h_r + v_\rho n \tau}\right)} \\
& \quad \frac{M_0 \cos[P(\theta' + \omega_m n \tau - \varphi)]}{\sqrt{(x - R_i \sin \theta' + v_x n \tau)^2 + (y + h_r + R_i \cos \theta' + v_\rho n \tau)^2 + (z - z')^2}} R_i d\theta' dz' \\
\phi_m(x, y, z, \varphi) = & + \frac{1}{4\pi} \sum_{n=0}^{\infty} \int_{-W_r/2}^{W_r/2} \int_{\arctan\left(\frac{x+v_x(n+1)\tau}{y+h_r + v_\rho n \tau}\right)}^{2\pi + \arctan\left(\frac{x+v_x(n+1)\tau}{y+h_r + v_\rho n \tau}\right)} \\
& \quad \frac{M_0 \cos[P(\theta' + \omega_m n \tau - \varphi)]}{\sqrt{(x - R_i \sin \theta' + v_x(n+1)\tau)^2 + (y + h_r + R_i \cos \theta' + v_\rho n \tau)^2 + (z - z')^2}} R_i d\theta' dz' \\
& + \frac{1}{4\pi} \sum_{n=0}^{\infty} \int_{-W_r/2}^{W_r/2} \int_{\arctan\left(\frac{x+v_x n \tau}{y+h_r + v_\rho n \tau}\right)}^{2\pi + \arctan\left(\frac{x+v_x n \tau}{y+h_r + v_\rho n \tau}\right)} \\
& \quad \frac{M_0 \cos[P(\theta' + \omega_m n \tau - \varphi)]}{\sqrt{(x - R_o \sin \theta' + v_x n \tau)^2 + (y + h_r + R_o \cos \theta' + v_\rho n \tau)^2 + (z - z')^2}} R_o d\theta' dz' \\
& - \frac{1}{4\pi} \sum_{n=0}^{\infty} \int_{-W_r/2}^{W_r/2} \int_{\arctan\left(\frac{x+v_x(n+1)\tau}{y+h_r + v_\rho n \tau}\right)}^{2\pi + \arctan\left(\frac{x+v_x(n+1)\tau}{y+h_r + v_\rho n \tau}\right)} \\
& \quad \frac{M_0 \cos[P(\theta' + \omega_m n \tau - \varphi)]}{\sqrt{(x - R_o \sin \theta' + v_x(n+1)\tau)^2 + (y + h_r + R_o \cos \theta' + v_\rho n \tau)^2 + (z - z')^2}} R_o d\theta' dz'
\end{aligned} \tag{25}$$

Since the steps are infinitesimal, it can be replaced by integrals over time, given by:

$$\begin{aligned}
& - \frac{1}{4\pi\tau} \int_0^\infty \int_{-W_r/2}^{W_r/2} \int_{R_i}^{R_o} \int_{\arctan\left(\frac{x+v_x t}{y+h_r+v_\rho t}\right)}^{2\pi+\arctan\left(\frac{x+v_x t}{y+h_r+v_\rho t}\right)} \\
& \quad \frac{M_0 \cos^{P(\theta'+\omega_m t-\varphi)}(1-P)}{\sqrt{(x-\rho' \sin \theta' + v_x t)^2 + (y+h_r + \rho' \cos \theta' + v_\rho t)^2 + (z-z')^2}} d\theta' d\rho' dz' dt \\
& + \frac{1}{4\pi\tau} \int_0^\infty \int_{-W_r/2}^{W_r/2} \int_{R_i}^{R_o} \int_{\arctan\left(\frac{x+v_x t+v_x \tau}{y+h_r+v_\rho t}\right)}^{2\pi+\arctan\left(\frac{x+v_x t+v_x \tau}{y+h_r+v_\rho t}\right)} \\
& \quad \frac{M_0 \cos^{P(\theta'+\omega_m t-\varphi)}(1-P)}{\sqrt{(x-\rho' \sin \theta' + v_x t + v_x \tau)^2 + (y+h_r + \rho' \cos \theta' + v_\rho t)^2 + (z-z')^2}} d\theta' d\rho' dz' dt \\
& - \frac{1}{4\pi\tau} \int_0^\infty \int_{-W_r/2}^{W_r/2} \int_{\arctan\left(\frac{x+v_x t}{y+h_r+v_\rho t}\right)}^{2\pi+\arctan\left(\frac{x+v_x t}{y+h_r+v_\rho t}\right)} \\
& \quad \frac{M_0 \cos[P(\theta'+\omega_m t-\varphi)]}{\sqrt{(x-R_i \sin \theta' + v_x t)^2 + (y+h_r + R_i \cos \theta' + v_\rho t)^2 + (z-z')^2}} R_i d\theta' dz' dt \\
\phi_m(x, y, z, \varphi) = & + \frac{1}{4\pi\tau} \int_0^\infty \int_{-W_r/2}^{W_r/2} \int_{\arctan\left(\frac{x+v_x t+v_x \tau}{y+h_r+v_\rho t}\right)}^{2\pi+\arctan\left(\frac{x+v_x t+v_x \tau}{y+h_r+v_\rho t}\right)} \\
& \quad \frac{M_0 \cos[P(\theta'+\omega_m t-\varphi)]}{\sqrt{(x-R_i \sin \theta' + v_x t + v_x \tau)^2 + (y+h_r + R_i \cos \theta' + v_\rho t)^2 + (z-z')^2}} R_i d\theta' dz' dt \\
& + \frac{1}{4\pi\tau} \int_0^\infty \int_{-W_r/2}^{W_r/2} \int_{\arctan\left(\frac{x+v_x t}{y+h_r+v_\rho t}\right)}^{2\pi+\arctan\left(\frac{x+v_x t}{y+h_r+v_\rho t}\right)} \\
& \quad \frac{M_0 \cos[P(\theta'+\omega_m t-\varphi)]}{\sqrt{(x-R_o \sin \theta' + v_x t)^2 + (y+h_r + R_o \cos \theta' + v_\rho t)^2 + (z-z')^2}} R_o d\theta' dz' dt \\
& - \frac{1}{4\pi\tau} \int_0^\infty \int_{-W_r/2}^{W_r/2} \int_{\arctan\left(\frac{x+v_x t+v_x \tau}{y+h_r+v_\rho t}\right)}^{2\pi+\arctan\left(\frac{x+v_x t+v_x \tau}{y+h_r+v_\rho t}\right)} \\
& \quad \frac{M_0 \cos[P(\theta'+\omega_m t-\varphi)]}{\sqrt{(x-R_o \sin \theta' + v_x t + v_x \tau)^2 + (y+h_r + R_o \cos \theta' + v_\rho t)^2 + (z-z')^2}} R_o d\theta' dz' dt
\end{aligned} \tag{26}$$

Since each pair of the charge and counter charge integrals is only off by an infinitesimal $v_x \tau$ component, if $f(t)$ is continuous, smooth and differentiable with respect to t , the difference between the two can be approximated by linearization.

$$f(t) - f(t + v_x \tau) \approx f(t) - f(t) - \frac{\partial f(t)}{\partial t} v_x \tau = -\frac{\partial f(t)}{\partial t} v_x \tau \tag{27}$$

We can bypass redundant calculations by considering:

$$\int_0^\infty \frac{\partial f(x, y, z, t, \varphi)}{\partial t} dt = [f(x, y, z, t, \varphi)]_{t=0}^{t=\infty} \tag{28}$$

The simplified form of equation (26) is then written as:

$$\phi_m(x, y, z, \varphi) \approx \frac{v_x M_0}{4\pi} \left[\begin{array}{l} \int_{-W_r/2}^{W_r/2} \int_{R_i}^{R_o} \int_{\arctan(\frac{x+v_x t}{y+h_r+v_\rho t})}^{2\pi + \arctan(\frac{x+v_x t}{y+h_r+v_\rho t})} \cos^{P(\theta' + \omega_m t - \varphi)}(1-P) \\ \frac{d\theta' d\rho' dz'}{\sqrt{(x - \rho' \sin \theta' + v_x t)^2 + (y + h_r + \rho' \cos \theta' + v_\rho t)^2 + (z - z')^2}} \\ + \int_{-W_r/2}^{W_r/2} \int_{\arctan(\frac{x+v_x t}{y+h_r+v_\rho t})}^{2\pi + \arctan(\frac{x+v_x t}{y+h_r+v_\rho t})} \cos[P(\theta' + \omega_m t - \varphi)] \\ \frac{d\theta' d\rho' dz'}{\sqrt{(x - R_i \sin \theta' + v_x t)^2 + (y + h_r + R_i \cos \theta' + v_\rho t)^2 + (z - z')^2}} R_i d\theta' dz' \\ - \int_{-W_r/2}^{W_r/2} \int_{\arctan(\frac{x+v_x t}{y+h_r+v_\rho t})}^{2\pi + \arctan(\frac{x+v_x t}{y+h_r+v_\rho t})} \cos[P(\theta' + \omega_m t - \varphi)] \\ \frac{d\theta' d\rho' dz'}{\sqrt{(x - R_o \sin \theta' + v_x t)^2 + (y + h_r + R_o \cos \theta' + v_\rho t)^2 + (z - z')^2}} R_o d\theta' dz' \end{array} \right]_{t=0}^{t=\infty} \quad (29)$$

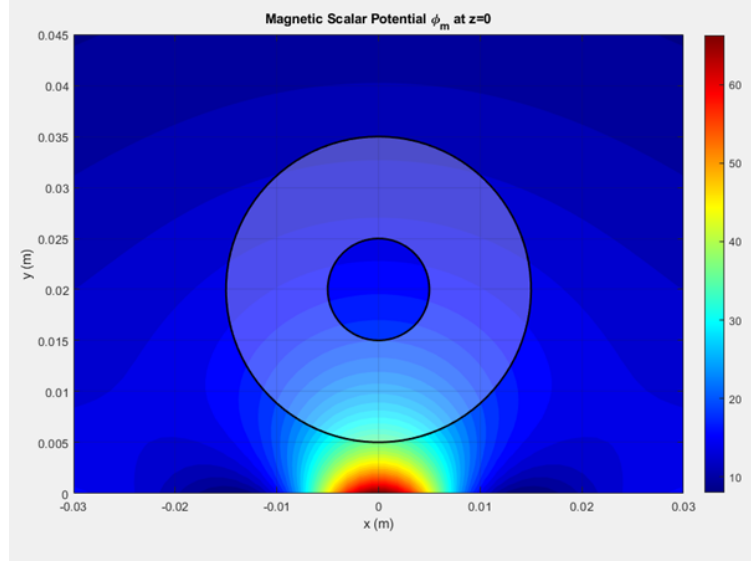


Figure 14: Magnetic scalar potential distribution contributed by the image external rotor in steady state, where the black circle indicates the position of the Halbach rotor

The total magnetic force acting on the volume and surface charge is given by:

$$\vec{F}_m = -\mu_0 \left(\iiint_{\tau'} \rho_m \vec{\nabla} \phi_m d\tau' + \iint_{a'} \sigma_m \vec{\nabla} \phi_m da' \right) \quad (30)$$

By substituting the derived parameters, the following results:

$$\begin{aligned}
\vec{F}_m = -\mu_0 \left\{ & - \int_{-W_r/2}^{W_r/2} \int_0^{2\pi} \int_{R_i}^{R_o} M_0 \cos^{P(\theta-\varphi)} (1-P) \right. \\
& \times \left[\left(\frac{\partial}{\partial x} \hat{i} + \frac{\partial}{\partial y} \hat{j} \right) \phi_m(x, y, z, \varphi) \right] \Big|_{\substack{x=\rho \sin \theta \\ y=h_r+\rho \cos \theta}} d\rho d\theta dz \\
& - \int_{-W_r/2}^{W_r/2} \int_0^{2\pi} M_0 \cos[P(\theta-\varphi)] \\
& \times \left[\left(\frac{\partial}{\partial x} \hat{i} + \frac{\partial}{\partial y} \hat{j} \right) \phi_m(x, y, z, \varphi) \right] \Big|_{\substack{x=R_i \sin \theta \\ y=h_r+R_i \cos \theta}} R_i d\theta dz \\
& + \int_{-W_r/2}^{W_r/2} \int_0^{2\pi} M_0 \cos[P(\theta-\varphi)] \\
& \times \left[\left(\frac{\partial}{\partial x} \hat{i} + \frac{\partial}{\partial y} \hat{j} \right) \phi_m(x, y, z, \varphi) \right] \Big|_{\substack{x=R_o \sin \theta \\ y=h_r+R_o \cos \theta}} R_o d\theta dz \left. \right\} \quad (31)
\end{aligned}$$

The z component is neglected due to axial symmetry.

The result shows an oscillation of force with period $T = \pi/P$ as illustrated in the below graph.

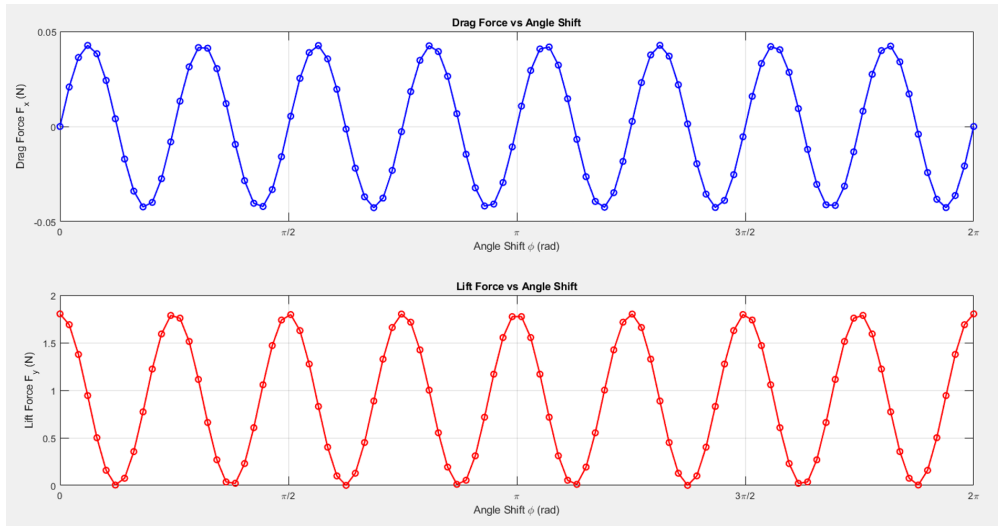


Figure 15: Graph of steady state x and y force components over angle shift

3.4 Model Evaluation

The use of magnetic charge to derive the exact source field is extremely useful for facilitating the thin sheet approximation and avoid tedious 3D calculations. It gives a good approximation of the field components. However, the sources field is too overly complicated that it is not applicable for thick plate analysis.

4 3-D Laplace-Poisson Approach – Magnetic Scalar Potential Model

In this section, we will utilize the Laplace-Poisson equation to analyse the magnetic scalar potential of the Halbach rotor. The homogeneous Helmholtz equation is applicable in regions where there is no magnetic source, and the nonhomogeneous Helmholtz equation will be employed in regions where magnetic sources are present.

Several papers have investigated the magnetic source field generated by the Halbach rotor. However, only a two-dimensional general equation for this magnetic source field has been derived [31]. A few studies have attempted to solve it using the finite element method [7, 8, 13], which provides great insights and accurate calculations, but this limits future exploration due to the absence of equations for tuning the parameters. In this section, we are going to expand to the 3-dimensional field by considering the edge effect.

4.1 Governing Parameters and Equations

4.1.1 Region Definition

We separate the space into four regions: the air space region inside the rotor Ω_I , magnet region Ω_{II} , and air space region elsewhere Ω_{III} and Ω_{IV} , each corresponds to different singularity points. Since the Halbach rotor exhibits axial symmetry, we can simplify the analysis by focusing exclusively on the region where $z \geq 0$. Therefore, the range of the regions is:

$$\Omega_I \in \{\rho \leq R_i \cup 0 \leq z \leq W_r/2\} \quad (32)$$

$$\Omega_{II} \in \{R_i \leq \rho \leq R_o \cup 0 \leq z \leq W_r/2\} \quad (33)$$

$$\Omega_{III} \in \{\rho \leq R_o \cup W_r/2 \leq z\} \quad (34)$$

$$\Omega_{IV} \in \{R_o \leq \rho \cup 0 \leq z\} \quad (35)$$

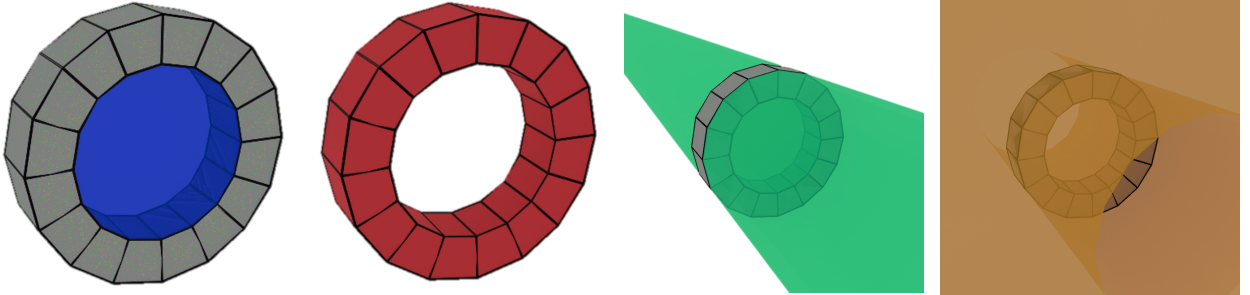


Figure 16: *
Region I (blue)

Figure 17: *
Region II (red)

Figure 18: *
Region III (green)

Figure 19: *
Region IV (orange)

Figure 20: Indications of regions I–IV

4.1.2 Parameter Address

The magnetic field is related to the magnetic field strength \vec{H} and the magnetisation \vec{M} by:

$$\vec{B} = \begin{cases} \mu_0(\vec{H} + \vec{M}), & R_i \leq \rho \leq R_o \cup 0 \leq z \leq W_r/2 \\ \mu_0\vec{H}, & \text{otherwise} \end{cases} \quad (36)$$

By performing divergence on both sides of the equation, by Maxwell's equation, the LHS reduces to zero since $\vec{\nabla} \cdot \vec{B} = 0$. Therefore, the magnetization and magnetic field strength are related by:

$$\vec{\nabla} \cdot \vec{H} = -\vec{\nabla} \cdot \vec{M} \quad (37)$$

The magnetic scalar potential and the magnetic field strength are related by:

$$\vec{H} = -\vec{\nabla}\phi_m = -\left(\frac{\partial\phi_m}{\partial\rho}\hat{\rho} + \frac{1}{\rho}\frac{\partial\phi_m}{\partial\theta}\hat{\theta} + \frac{\partial\phi_m}{\partial z}\hat{z}\right) \quad (38)$$

By applying divergence to both sides of the equation, a Poisson equation is obtained in which the magnetization serves as a source for the magnetic field:

$$\nabla^2\phi_m = \vec{\nabla} \cdot \vec{M} \quad (39)$$

Recall the magnetization derived in Section 2. Since the dimension of the radial term of the rotor is no longer negligible in this context, the region where the magnetization occurs is included:

$$\vec{M}(\rho, \theta, z) = \begin{cases} M_0 [\cos(P\theta)\hat{\rho} \mp \sin(P\theta)\hat{\theta}], & R_i \leq \rho \leq R_o \cup 0 \leq z \leq W_r/2 \\ 0, & \text{otherwise} \end{cases} \quad (40)$$

By substituting it in equation (39), we obtain an expression for the magnetic scalar potential in different regions:

$$\nabla^2\phi_{m\varsigma}(\rho, \theta, z) = \frac{1}{\rho}\frac{\partial}{\partial\rho}\left(\rho\frac{\partial\phi_{m\varsigma}}{\partial\rho}\right) + \frac{1}{\rho^2}\frac{\partial^2\phi_{m\varsigma}}{\partial\theta^2} + \frac{\partial^2\phi_{m\varsigma}}{\partial z^2} = 0, \quad \varsigma \in \{I, III, IV\} \quad (41)$$

$$\nabla^2\phi_{m\varsigma}(\rho, \theta, z) = \frac{1}{\rho}\frac{\partial}{\partial\rho}\left(\rho\frac{\partial\phi_{m\varsigma}}{\partial\rho}\right) + \frac{1}{\rho^2}\frac{\partial^2\phi_{m\varsigma}}{\partial\theta^2} + \frac{\partial^2\phi_{m\varsigma}}{\partial z^2} = \vec{\nabla} \cdot \vec{M}, \quad \varsigma \in \{II\} \quad (42)$$

Where the divergence of the magnetization vector in cylindrical coordinates is given by:

$$\vec{\nabla} \cdot \vec{M}(\rho, \theta) = \begin{cases} \frac{1}{\rho}M_0 \cos(P\theta)(1 \mp P), & R_i \leq \rho \leq R_o \cup 0 \leq z \leq W_r/2 \\ 0, & \text{otherwise} \end{cases} \quad (43)$$

4.2 Boundary Conditions

The Dirichlet boundary conditions at the singularity points should be considered. Given that the system exhibits angular symmetry ($P \in \mathbb{Z}^+ > 1$), the contribution of the magnetic scalar potential should approach zero at $\rho = 0$:

$$\phi_{mI}(0, \theta, z) = 0, \quad \phi_{mIII}(0, \theta, z) = 0 \quad (44)$$

The magnetic scalar potential should vanish at infinity. Therefore, the equations below can be written:

$$\lim_{z \rightarrow \infty} \phi_{mIII}(\rho, \theta, z) = 0, \quad \lim_{\rho \rightarrow \infty} \phi_{mIV}(\rho, \theta, z) = \lim_{z \rightarrow \infty} \phi_{mIV}(\rho, \theta, z) = 0 \quad (45)$$

4.3 General Form of the Source Field

We start by employing the method of separation of variables and express the magnetic scalar potential as follows:

$$\phi_m(\rho, \theta, z) = R(\rho)\Theta(\theta)Z(z) \quad (46)$$

From section 3, we can observe that the angular dependency only includes $\cos(P\theta)$. Therefore, the homogeneous equation has the form:

$$\phi_m(\rho, \theta, z) = \cos(P\theta)R(\rho)Z(z) \quad (47)$$

We assign an eigenvalue λ_n to the z component, expressed as:

$$\partial_{zz}Z_{\varsigma,h}(z) = \pm\lambda_n^2Z_{\varsigma,h}(z) \quad (48)$$

The set of solutions is given by:

$$\phi_{m\varsigma}(\rho, \theta, z) = \cos(P\theta) \begin{cases} \sum_{n=1}^{\infty} [a_1 J_P(\lambda_n \rho) + b_1 Y_P(\lambda_n \rho)](c_1 e^{\lambda_n z} + d_1 e^{-\lambda_n z}) \\ \sum_{n=1}^{\infty} [a_1 I_P(\lambda_n \rho) + b_1 K_P(\lambda_n \rho)][c_1 \sin(\lambda_n z) + d_1 \cos(\lambda_n z)] \end{cases} \quad (49)$$

Where J_P , Y_P , I_P and K_P are the Bessel functions of the first kind, second kind, Bessel modified functions of the first and second kind, respectively.

The particular solution can be found by substituting $\phi_{mII} = M\rho \cos(P\theta)$ into the equation of Ω_{II} . We can see that:

$$\phi_{mII,p} = \frac{M_0(1 \mp P)}{1 - P^2} \rho \cos(P\theta) \quad (50)$$

Where:

$$\nabla^2 \phi_{mII,p} = \vec{\nabla} \cdot \vec{M} \quad (51)$$

By considering the boundary conditions at each singularity points, the general form of the governing equations of each region is derived:

$$\phi_I = \cos(P\theta) \left[\sum_{n=1}^{\infty} C_{I1}(n) e^{-k_{In}z} J_P(k_n \rho) \right] \quad (52)$$

$$\phi_{II} = \cos(P\theta) \left[M\rho + \sum_{n=1}^{\infty} C_{II1}(n) \cos(k_{In}z) I_P(k_{In}\rho) \right. \\ \left. + \sum_{n=1}^{\infty} C_{II2}(n) \cos(k_{In}z) K_P(k_{In}\rho) + \sum_{n=1}^{\infty} C_{II3}(n) e^{k_{In}z} J_P(k_{In}\rho) \right. \\ \left. + \sum_{n=1}^{\infty} C_{II4}(n) e^{k_{In}z} Y_P(k_{In}\rho) + \sum_{n=1}^{\infty} C_{II5}(n) e^{-k_{In}z} J_P(k_{In}\rho) \right. \\ \left. + \sum_{n=1}^{\infty} C_{II6}(n) e^{-k_{In}z} Y_P(k_{In}\rho) \right] \quad (53)$$

$$\phi_{III} = \cos(P\theta) \left[\sum_{n=1}^{\infty} C_{III1}(n) e^{-k_{IIIIn}z} J_P(k_{IIIIn}\rho) \right] \quad (54)$$

$$\phi_{IV} = \cos(P\theta) \left[\sum_{n=1}^{\infty} C_{IV1}(n) e^{-k_{IVn}z} J_P(k_{IVn}\rho) + \sum_{n=1}^{\infty} C_{IV2}(n) e^{-k_{IVn}z} Y_P(k_{IVn}\rho) \right] \quad (55)$$

Where $M = \frac{M_0(1 \mp P)}{1 - P^2}$ and $C_{I1}(n)$ to $C_{IV2}(n)$ are the 10 undetermined series of constants.

4.4 Solving with Hybrid Analytical-Numerical Method

In this section, we will utilize the Orthogonal Greedy Algorithm [21, 30] to compute the numerical value of the coefficients.

4.4.1 Failing of Pure Analytic Model

The determination of the coefficients in the infinite sum depends on the self-adjointness of the functions. For a second-order differential equation given by:

$$L[u(x)] = \frac{d}{dx} \left[p(x) \frac{du(x)}{dx} \right] + q(x)u(x) = -\lambda \omega(x)u(x) \quad (56)$$

To let the function be self-adjoint, the Robin boundary condition should be satisfied over the region of interest $[a, b]$, denoted as:

$$\left[p(x) \left(v(x) \frac{du(x)}{dx} - u(x) \frac{dv(x)}{dx} \right) \right]_a^b = 0 \quad (57)$$

This requires selecting an appropriate eigenvalue. However, given that the problem is two-dimensional (disregarding angular dependence), choosing fixed eigenvalues for both dimensions does not ensure self-adjointness in both directions. Additionally, the differential operators involving exponential functions and modified Bessel functions yield negative eigenvalues, which are not suitable for eigen decomposition. These characteristics disallow solving for the coefficients in a traditional way.

4.4.2 Orthogonal Greedy Algorithm

The table below shows the parameters used in the approximation.

Table 3: Parameters for Orthogonal Greedy Algorithm

Parameter	Definition	Dimension
N	Total collection points	\mathbb{R}^1
n	The size of the eigenvalue (wave number) set	\mathbb{R}^1
κ	Basis type	\mathbb{R}^1
$\vec{\phi}_e$	Exact solution obtained from equation (8)	\mathbb{R}^N
B	Basis Matrix	$\mathbb{R}^{N \times n}$
C	Coefficient Vector	\mathbb{R}^n
ϵ	Relative RMS error	\mathbb{R}^1
ϵ_{target}	Target relative RMS error	\mathbb{R}^1
ϵ_{ortho}	Orthogonality threshold	\mathbb{R}^1

Construction of Basis Matrix For each iteration, if there exists, a new basis of type κ with eigenvalue k_n will be added to the basis matrix:

$$B^{(n)} = [b_{\kappa 1} \ b_{\kappa 2} \ \dots \ b_{\kappa n}] \quad (58)$$

Where $b_{\kappa n}$ is type κ basis $N \times 1$ vector with eigenvalue k_n evaluated on all the collection points.

Choice of Orthogonal Basis The basis matrix is decomposed via singular value decomposition (SVD), given by [6, 28, 27]:

$$B^{(n)} = U^{(n)} \Sigma^{(n)} (V^{(n)})^T \quad (59)$$

Where $r = \text{rank}(B^{(n)})$, $U^{(n)} \in \mathbb{R}^{N \times r}$, $\Sigma^{(n)} = \text{diag}(\sigma_1, \sigma_2, \dots, \sigma_r)$ and $V^{(n)} \in \mathbb{R}^{r \times n}$.

The column space projection of the matrix $B^{(n)}$ is given by:

$$P^{(n)} = U^{(n)} (U^{(n)})^T \quad (60)$$

For a new candidate vector \vec{v} , its orthogonal component with respect to the matrix $B_\kappa^{(n)}$ is given by:

$$\vec{v}_\perp = (I - U^{(n)} (U^{(n)})^T) \vec{v} \quad (61)$$

Our goal is to find vectors that can form a new basis to avoid redundant basis. Therefore, we will accept the candidate vector \vec{v} if the ratio of the Euclidean norm of the orthogonal term and the whole term exceeds the threshold ϵ_{ortho} , denoted as:

$$\frac{\|\vec{v}_\perp\|}{\|\vec{v}\|} > \epsilon_{\text{ortho}} \quad (62)$$

If (62) is satisfied, the new Basis matrix will become:

$$B^{(n+1)} = [B^{(n)} \ \vec{v}] \quad (63)$$

Find Coefficient Vector Through Residue Minimization The Residue at the n^{th} iteration is defined as:

$$\vec{r}_n = B^{(n)} C^{(n)} - \vec{\phi}_e \quad (64)$$

The coefficient matrix is obtained by solving the regularized least square problem using Tikhonov regularization [14, 16]:

$$C^{(n)} = \arg \min \left\{ \|B^{(n)} C^{(n)} - \vec{\phi}_e\|^2 + \lambda^2 \|C^{(n)}\|^2 \right\} \quad (65)$$

The term $\lambda^2 \|C^{(n)}\|^2$ is a penalty term used for punishing large coefficients term to prevent overfitting.

Denote:

$$M(C^{(n)}) = \|B^{(n)}C^{(n)} - \vec{\phi}_e\|^2 + \lambda^2\|C^{(n)}\|^2 \quad (66)$$

By expanding the terms, we arrive:

$$\begin{aligned} M(C^{(n)}) &= (B^{(n)}C^{(n)} - \vec{\phi}_e)^T(B^{(n)}C^{(n)} - \vec{\phi}_e) + \lambda^2(C^{(n)})^T(C^{(n)}) \\ &= (C^{(n)})^T(B^{(n)})^T B^{(n)} C^{(n)} - 2(C^{(n)})^T(B^{(n)})^T \vec{\phi}_e + \vec{\phi}_e^T \vec{\phi}_e + \lambda^2(C^{(n)})^T C^{(n)} \end{aligned} \quad (67)$$

By performing matrix derivatives:

$$\frac{dM}{dC^{(n)}} = 2(B^{(n)})^T B^{(n)} C^{(n)} - 2(B^{(n)})^T \vec{\phi}_e + 2\lambda^2 C^{(n)} \quad (68)$$

Setting the derivative to 0 gives us the following coefficient matrix:

$$C^{(n)} = V^{(n)}(\Sigma^{(n)2} + \lambda^2 I)^{-1}\Sigma^{(n)}(U^{(n)})^T \vec{\phi}_e \quad (69)$$

$(\Sigma^{(n)2} + \lambda^2 I)^{-1}\Sigma^{(n)}$ is a diagonal matrix where its i^{th} diagonal element is evaluated as:

$$\frac{\sigma_i}{\sigma_i^2 + \lambda^2} \quad (70)$$

The algorithm will continue to run until the target RMS error is reached, denoted as:

$$\epsilon = \frac{\|\vec{r}_{n+1}\|}{\|\vec{\phi}_e\|} < \epsilon_{\text{target}} \quad (71)$$

The detailed results and the MATLAB code will be provided in Appendix 3.

4.5 Implementation and Results of the Hybrid Analytical-Numerical Method

We implemented the algorithm for the external configuration of the Halbach rotor.

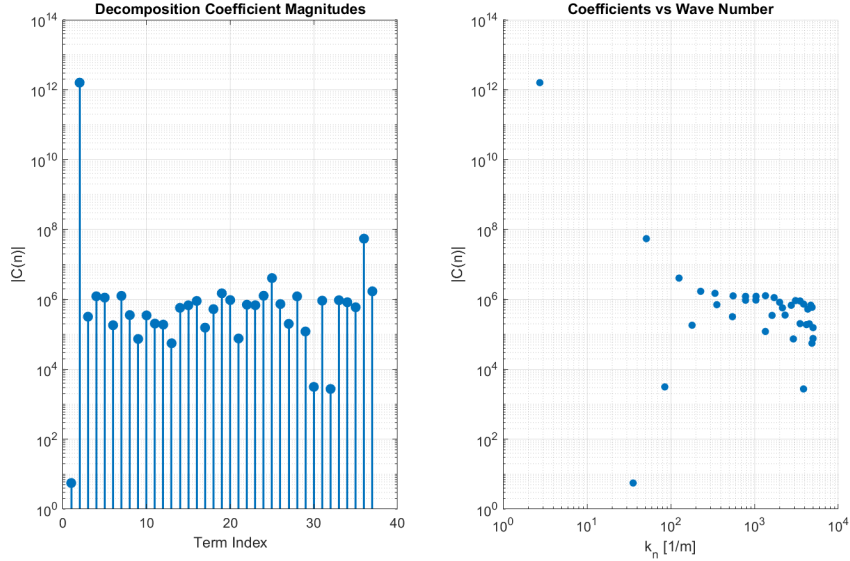


Figure 21: Illustration of the coefficient's magnitude against wave number and basis type for both internal and external rotor in Ω_{IV}

4.6 Overall Evaluation

4.6.1 Advantages Over Pure Analytical and Numerical Model

This study introduces a robust 3-D analytical-numerical framework for modelling the magnetic scalar potential of a Halbach rotor using the Laplace-Poisson approach. The model goes beyond conventional 2-D analyses.

In contrast to traditional analytical models, this approach employs a hybrid methodology that combines analytical functions with algorithms for numerical coefficients. This enables analysis of the field in a frequency context. Additionally, the analytical model facilitates extensive analysis across various coordinate points and systems, offering greater analytical flexibility compared to standard numerical methods.

4.6.2 Future Works

A pure analytical model is not derived as it failed for the non-self-adjointness and negative eigenvalues. This can be proven by our numerical results, as the chosen eigenvalues show different behaviours and properties in different regions that differ from traditional eigenvalue selection. Further investment should be examined such that we can construct complicated analytic models in a 3D sense.

5 Governing Equations for Magnetic Source on Conductive Plate

The model is divided into three regions: Ω_1 , Ω_2 , and Ω_3 , as shown in the graph below. Here, Ω_2 represents the conductive region, while Ω_1 and Ω_3 are the areas above and below the conductive plate, respectively. We denote the boundaries between the regions as Γ_1 and Γ_2 for the analysis of boundary conditions. We employ a moving coordinate system relative to the rotor, with the origin positioned at the center of the rotor.

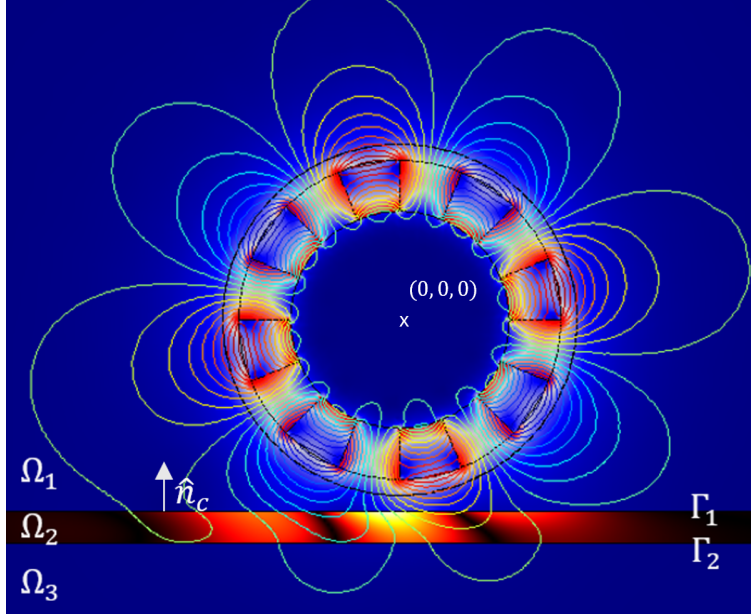


Figure 22: Illustration of the boundary of an external operating Halbach rotor modified from [5]

The following table denotes the magnetic components used in the analysis.

Table 4: Magnetic Components for Conductive Plate Analysis

Parameter	Description	Region
\vec{B}^s	Source field of the Halbach rotor	Ω_1
\vec{A}	Magnetic vector potential	Ω_2
ϕ_n	Magnetic scalar potential	Ω_1, Ω_3

5.1 Conductive Plate Region

Using the differential form of Maxwell's equation,

$$\vec{\nabla} \times (\vec{\nabla} \times \vec{A}) = \mu_0 \sigma (\vec{E} + \vec{v} \times \vec{B}) \quad (72)$$

$$\vec{E} = -\vec{\nabla}V - \frac{\partial \vec{A}}{\partial t} \quad (73)$$

Considering the Coulomb gauge $\vec{\nabla} \cdot \vec{A} = 0$ and setting the gradient of electric potential to 0, this equation is obtained [17]:

$$\nabla^2 \vec{A} = \mu_0 \sigma \left(\frac{\partial \vec{A}}{\partial t} + (\vec{v} \cdot \vec{\nabla}) \vec{A} \right) \quad (74)$$

Where \vec{v} is the translational velocity of the magnetic source. The term $\frac{\partial \vec{A}}{\partial t} + (\vec{v} \cdot \vec{\nabla}) \vec{A}$ is the convective derivative of \vec{A} , written as the total time derivative $\frac{d\vec{A}}{dt}$. It represents the rate of change of magnetic vector

potential at the moving location of the particle for time [15]. The motional effect of the magnetic source moving above the conductive plate can be described by this convective-diffusion equation [7].

To account for the time component, we can separate the source angular velocity by

$$\vec{A}(x, y, z, t) = \vec{A}(x, y, z)e^{i\omega_e t} \quad (75)$$

Where ω_e is the magnetic source frequency. It is related to the angular velocity of the Halbach rotor ω_m from Bird and Lipo (2008):

$$\omega_m = \frac{\omega_e}{P} \quad (76)$$

Where P is the number of pole pairs of the Halbach rotor. By substituting (75) into the differential equation (74) and assuming the rotor travels along the x axis,

$$\nabla^2 \vec{A} = \mu_0 \sigma \left(i\omega_e \vec{A} + v_x \frac{\partial \vec{A}}{\partial x} \right), \quad \text{in } \Omega_2 \quad (77)$$

5.2 Non-conductive Region

Considering the eddy current and the induced magnetic field, we can express the total magnetic field as the sum of the sources [22]:

$$\vec{B}(x, y, z, t) = \vec{B}^s(x, y, z, t) + \vec{B}^r(x, y, z, t) \quad (78)$$

Where \vec{B}^s is the magnetic source from the Halbach Rotor and \vec{B}^r is the magnetic source from the induced eddy current. The induced source can be further expressed in terms of the magnetic scalar potential ϕ_n :

$$\vec{B}^r = -\mu_0 \vec{\nabla} \phi_n, \quad n \in \{1, 3\} \quad (79)$$

Where n corresponds to the marked number of the non-conducting region. By taking the divergence from both sides in Maxwell's equation $\vec{\nabla} \cdot \vec{B} = 0$, an equation for the magnetic scalar potential is obtained:

$$\nabla^2 \phi_n = 0 \quad (80)$$

The time-dependent term equivalent to equation (75) can be further separated:

$$\phi_n(x, y, z, t) = \phi_n(x, y, z)e^{i\omega_e t} \quad (81)$$

5.3 Boundary Conditions

In this section, to simplify calculations, the magnetic permittivity is assumed to be the same as the one located in vacuum for both the air and the conductive plate, i.e., $\mu = \mu_0$. $\vec{B}^s(x, y, z, t)$, $\vec{B}^r(x, y, z, t)$, $\vec{B}^t(x, y, z, t)$ are denoted as the incident (source), reflected (induced by eddy current), and transmitted magnetic field, respectively. By considering the boundary conditions on Γ_1 ,

$$\vec{B}^t(x, -h_r, z, t) = \vec{B}^s(x, -h_r, z, t) + \vec{B}^r(x, -h_r, z, t) \quad (82)$$

Where h_r is the height of the rotor above the conductive plate. Rewriting it in terms of the magnetic vector and scalar potential in each direction of the boundary Γ_1 :

$$\left. \frac{\partial \vec{A}_z(x, y, z, t)}{\partial y} \right|_{y=-h_r} - \left. \frac{\partial \vec{A}_y(x, -h_r, z, t)}{\partial z} \right|_{y=-h_r} = \vec{B}_x^s(x, -h_r, z, t) - \mu_0 \left. \frac{\partial \phi_1(x, -h_r, t)}{\partial x} \right|_{y=-h_r} \quad (83)$$

$$\left. \frac{\partial \vec{A}_x(x, -h_r, z, t)}{\partial z} \right|_{y=-h_r} - \left. \frac{\partial \vec{A}_z(x, -h_r, z, t)}{\partial x} \right|_{y=-h_r} = \vec{B}_y^s(x, -h_r, z, t) - \mu_0 \left. \frac{\partial \phi_1(x, y, t)}{\partial y} \right|_{y=-h_r} \quad (84)$$

$$\left. \frac{\partial \vec{A}_y(x, -h_r, z, t)}{\partial x} \right|_{y=-h_r} - \left. \frac{\partial \vec{A}_x(x, y, z, t)}{\partial y} \right|_{y=-h_r} = \vec{B}_z^s(x, -h_r, z, t) - \mu_0 \left. \frac{\partial \phi_1(x, -h_r, t)}{\partial z} \right|_{y=-h_r} \quad (85)$$

Since there are no source fields located in Ω_3 , the boundary conditions for Γ_2 are

$$\frac{\partial \vec{A}_z(x, y, z, t)}{\partial y} \Big|_{y=-(h_r+d_p)} - \frac{\partial \vec{A}_y(x, -(h_r+d_p), z, t)}{\partial z} = -\mu_0 \frac{\partial \phi_3(x, -(h_r+d_p), t)}{\partial x} \quad (86)$$

$$\frac{\partial \vec{A}_x(x, -(h_r+d_p), z, t)}{\partial z} - \frac{\partial \vec{A}_z(x, -(h_r+d_p), z, t)}{\partial x} = -\mu_0 \frac{\partial \phi_3(x, y, t)}{\partial y} \Big|_{y=-(h_r+d_p)} \quad (87)$$

$$\frac{\partial \vec{A}_y(x, -(h_r+d_p), z, t)}{\partial x} - \frac{\partial \vec{A}_x(x, y, z, t)}{\partial y} \Big|_{y=-(h_r+d_p)} = -\mu_0 \frac{\partial \phi_3(x, -(h_r+d_p), t)}{\partial z} \quad (88)$$

It is assumed that the plate is long enough such that the magnetic field at the edge of the plate is zero:

$$\vec{B}(\pm L, y, \pm L, t) = 0 \quad (89)$$

Where L is the half-length of the plate.

To ensure the uniqueness of the solution [7, 1],

$$\hat{n}_c \cdot \vec{A} = 0, \quad \text{on } \Gamma_1, \Gamma_2 \quad (90)$$

Which automatically implies that

$$\hat{n}_c \cdot \vec{J} = 0, \quad \text{on } \Gamma_1, \Gamma_2 \quad (91)$$

Where \vec{J} is the eddy current density of the plate.

6 Fourier Analysis on Problem Region

To streamline the differential expressions of the problem region and the boundary equations, the Fourier transform in the spatial domain is employed (introduced in Paudel and Bird (2011)) after generalization in the 3D space domain.

The Fourier transformed spatial domain is given by

$$\tilde{A}(\xi, y, \zeta, t) = \int_{-\infty}^{\infty} \int_{-\infty}^{\infty} \vec{A}(x, y, z, t) e^{i\xi x} e^{i\zeta z} dx dz \quad (92)$$

$$\tilde{\phi}_n(\xi, y, \zeta, t) = \int_{-\infty}^{\infty} \int_{-\infty}^{\infty} \phi_n(x, y, z, t) e^{i\xi x} e^{i\zeta z} dx dz \quad (93)$$

6.1 Transformed Governing Equations

By considering (92), the transformed magnetic vector potential equation (77) in Ω_2 is given by

$$\frac{\partial^2 \tilde{A}}{\partial y^2} = \gamma^2 \tilde{A} \quad (94)$$

Where

$$\gamma^2 = \xi^2 + \zeta^2 + i\mu_0\sigma(\omega_e - v_x\xi) \quad (95)$$

The proof of the Fourier transformed differential term is given in Appendix 2.

Solving equation (94) gives

$$\tilde{A} = \begin{bmatrix} \alpha_x(\xi, \zeta)e^{\gamma y} + \beta_x(\xi, \zeta)e^{-\gamma y} \\ \alpha_y(\xi, \zeta)e^{\gamma y} + \beta_y(\xi, \zeta)e^{-\gamma y} \\ \alpha_z(\xi, \zeta)e^{\gamma y} + \beta_z(\xi, \zeta)e^{-\gamma y} \end{bmatrix} e^{i\omega_e t} \quad (96)$$

The same procedure is done on equation (80). By considering the boundary conditions in Ω_1 and Ω_3 , one will arrive at

$$\frac{\partial^2 \tilde{\phi}_n}{\partial y^2} = k^2 \tilde{\phi}_n \quad (97)$$

$$\tilde{\phi}_1(\xi, y, \zeta, t) = v(\xi, \zeta)e^{-ky} e^{i\omega_e t}, \quad \tilde{\phi}_3(\xi, y, \zeta, t) = \nu(\xi, \zeta)e^{ky} e^{i\omega_e t} \quad (98)$$

Where

$$k^2 = \xi^2 + \zeta^2 \quad (99)$$

6.2 Transformed Boundary Equations

The transformed boundary equations are

$$\gamma(\alpha_z e^{-\gamma h_r} - \beta_z e^{\gamma h_r}) - i\zeta(\alpha_y e^{-\gamma h_r} + \beta_y e^{\gamma h_r}) = \tilde{B}_x^s(\xi, y = -h_r, \zeta) - i\mu_0 \xi v e^{kh_r} \quad (100)$$

$$i\zeta(\alpha_x e^{-\gamma h_r} + \beta_x e^{\gamma h_r}) - i\xi(\alpha_z e^{-\gamma h_r} + \beta_z e^{\gamma h_r}) = \tilde{B}_y^s(\xi, y = -h_r, \zeta) + \mu_0 k v e^{kh_r} \quad (101)$$

$$i\xi(\alpha_y e^{-\gamma h_r} + \beta_y e^{\gamma h_r}) - \gamma(\alpha_x e^{-\gamma h_r} - \beta_x e^{\gamma h_r}) = \tilde{B}_z^s(\xi, y = -h_r, \zeta) - i\mu_0 \zeta v e^{kh_r} \quad (102)$$

$$\gamma(\alpha_z e^{-\gamma(h_r+d_p)} - \beta_z e^{\gamma(h_r+d_p)}) - i\zeta(\alpha_y e^{-\gamma(h_r+d_p)} + \beta_y e^{\gamma(h_r+d_p)}) = -i\mu_0 \xi v e^{-k(h_r+d_p)} \quad (103)$$

$$i\zeta(\alpha_x e^{-\gamma(h_r+d_p)} + \beta_x e^{\gamma(h_r+d_p)}) - i\xi(\alpha_z e^{-\gamma(h_r+d_p)} + \beta_z e^{\gamma(h_r+d_p)}) = -\mu_0 k v e^{-k(h_r+d_p)} \quad (104)$$

$$i\xi(\alpha_y e^{-\gamma(h_r+d_p)} + \beta_y e^{\gamma(h_r+d_p)}) - \gamma(\alpha_x e^{-\gamma(h_r+d_p)} - \beta_x e^{\gamma(h_r+d_p)}) = -i\mu_0 \zeta v e^{-k(h_r+d_p)} \quad (105)$$

Where \tilde{B}^s is the Fourier transformed rotor source with time dependency excluded.

The transformed constraint (90) gives

$$\alpha_y(\xi, \zeta)e^{-\gamma h_r} + \beta_y(\xi, \zeta)e^{-\gamma h_r} = 0 \quad (106)$$

$$\alpha_y(\xi, \zeta)e^{-\gamma(h_r+d_p)} + \beta_y(\xi, \zeta)e^{-\gamma(h_r+d_p)} = 0 \quad (107)$$

The solved coefficients are provided in Appendix 4.

6.3 Gauge Transformation

To derive equation (74), the Coulomb gauge condition $\vec{\nabla} \cdot \vec{A} = 0$ was employed, and the gradient of the electric potential was assumed to be zero. As these initial assumptions may not be satisfied, a gauge transformation can be made to ensure consistency with the chosen gauge.

The gauge transform yields [15]

$$\vec{A}' = \vec{A} + \vec{\alpha}, \quad V' = V + \beta \quad (108)$$

Letting $\vec{\alpha} = \vec{\nabla}\lambda$ for some scalar function λ :

$$\vec{A}' = \vec{A} + \vec{\nabla}\lambda, \quad V' = V - \frac{\partial\lambda}{\partial t} \quad (109)$$

Where

$$\vec{\nabla} \left(\beta + \frac{\partial\lambda}{\partial t} \right) = 0, \quad \vec{\nabla} \times (\vec{\nabla}\lambda) = 0 \quad (110)$$

This ensures the electric field and magnetic field consistency respectively.

The transformed Coulomb gauge gives

$$-i\xi(\alpha_x(\xi, \zeta)e^{\gamma y} + \beta_x(\xi, \zeta)e^{-\gamma y}) - i\zeta(\alpha_z(\xi, \zeta)e^{\gamma y} + \beta_z(\xi, \zeta)e^{-\gamma y}) + \nabla^2\tilde{\lambda} = 0 \quad (111)$$

$$\tilde{\lambda} = \underbrace{Ae^{ky} + Be^{-ky}}_{\text{homogeneous}} + \underbrace{C_1e^{\gamma y} + C_2e^{-\gamma y}}_{\text{particular}} \quad (112)$$

Where $\tilde{\lambda}$ is the Fourier transformed scalar function, and

$$C_1 = \frac{i(\xi\alpha_x(\xi, \zeta) + \zeta\alpha_z(\xi, \zeta))}{\gamma^2 - k^2}, \quad C_2 = \frac{i(\xi\beta_x(\xi, \zeta) + \zeta\beta_z(\xi, \zeta))}{\gamma^2 - k^2} \quad (113)$$

The condition $\frac{\partial\lambda}{\partial t} = 0$ is automatically satisfied.

The coefficients of the homogeneous solution can be found by the boundary conditions (90), giving

$$\left. \frac{\partial\tilde{\lambda}}{\partial y} \right|_{y=-h_r} = 0, \quad \left. \frac{\partial\tilde{\lambda}}{\partial y} \right|_{y=-(h_r+d_p)} = 0 \quad (114)$$

The solved coefficients are

$$A = \frac{\gamma}{k \sinh(kd_p)} \left\{ C_2 e^{(k+\gamma)(h_r+d_p/2)} \sinh \left[\frac{(k-\gamma)d_p}{2} \right] - C_1 e^{(k-\gamma)(h_r+d_p/2)} \sinh \left[\frac{(k+\gamma)d_p}{2} \right] \right\} \quad (115)$$

$$B = \frac{\gamma}{k \sinh(kd_p)} \left\{ C_1 e^{-(k+\gamma)(h_r+d_p/2)} \sinh \left[\frac{(k-\gamma)d_p}{2} \right] - C_2 e^{-(k-\gamma)(h_r+d_p/2)} \sinh \left[\frac{(k+\gamma)d_p}{2} \right] \right\} \quad (116)$$

Therefore, the transformed vector potentials are

$$\tilde{A}'_x = \tilde{A}_x - i\xi\tilde{\lambda}, \quad \tilde{A}'_y = 0, \quad \tilde{A}'_z = \tilde{A}_z - i\zeta\tilde{\lambda} \quad (117)$$

The expression for the magnetic scalar potential in each region is obtained by applying the inverse Fourier transform.

$$\vec{A} = \frac{1}{4\pi^2} \begin{bmatrix} \int_{-\infty}^{\infty} \int_{-\infty}^{\infty} (\tilde{A}_x - i\xi\tilde{\lambda}) e^{-i\xi x} e^{-i\zeta z} d\xi d\zeta \\ 0 \\ \int_{-\infty}^{\infty} \int_{-\infty}^{\infty} (\tilde{A}_z - i\zeta\tilde{\lambda}) e^{-i\xi x} e^{-i\zeta z} d\xi d\zeta \end{bmatrix} \quad (118)$$

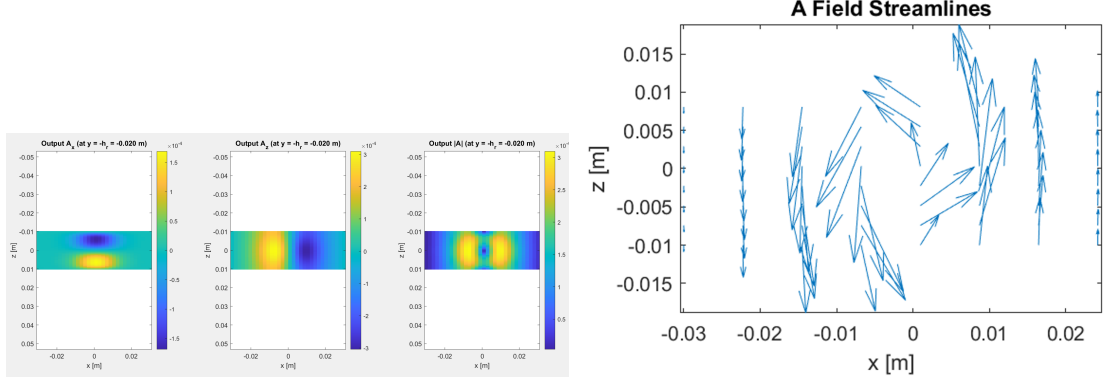


Figure 23: The magnetic vector potential on the conductive plate for (a) and (b) respectively

6.4 Magnetic Force

The components of the Maxwell stress tensor are expressed as [15]

$$T_{ij} = \frac{1}{\mu_0} \left(B_i B_j - \frac{1}{2} \delta_{ij} B^2 \right) \quad (119)$$

The total magnetic force is given by

$$\vec{F} = \underbrace{\iint_{a'} \vec{T} \cdot d\vec{a}'}_{\text{static force}} - \underbrace{\epsilon_0 \mu_0 \frac{d}{dt} \iiint_{\tau'} \vec{S} d\tau'}_{\text{loss}} \quad (120)$$

Where $d\vec{a}' = dx dz \hat{y}$ is the differential area vector of the plate. The loss term will average out to 0 in the steady state. The remaining components are

$$\vec{F} = \iint_{a'} \vec{T} \cdot d\vec{a}' \quad (121)$$

For the static force component, the force in each direction is expressed as

$$F_x = \frac{1}{\mu_0} \operatorname{Re} \left[\int_{-\infty}^{\infty} \int_{-\infty}^{\infty} B_x \bar{B}_y dx dz \right] \quad (122)$$

$$F_y = \frac{1}{2\mu_0} \operatorname{Re} \left[\int_{-\infty}^{\infty} \int_{-\infty}^{\infty} (B_y \bar{B}_y - B_x \bar{B}_x - B_z \bar{B}_z) dx dz \right], \quad \text{on } \Gamma_1 \quad (123)$$

The z direction force is neglected due to axial symmetry.

By applying Parseval's theorem, we can bypass the need for an additional inverse Fourier transform. The force components are now represented as

$$F_x = \frac{1}{4\pi^2 \mu_0} \operatorname{Re} \left[\int_{-\infty}^{\infty} \int_{-\infty}^{\infty} \tilde{B}_x \bar{\tilde{B}}_y d\xi d\zeta \right] \quad (124)$$

$$F_y = \frac{1}{8\pi^2 \mu_0} \operatorname{Re} \left[\int_{-\infty}^{\infty} \int_{-\infty}^{\infty} (\tilde{B}_y \bar{\tilde{B}}_y - \tilde{B}_x \bar{\tilde{B}}_x - \tilde{B}_z \bar{\tilde{B}}_z) d\xi d\zeta \right], \quad \text{on } \Gamma_1 \quad (125)$$

Where the transformed magnetic field is given by

$$\tilde{\vec{B}} = \begin{bmatrix} \frac{\partial \tilde{A}_z}{\partial y} & i(\xi \tilde{A}_z - \zeta \tilde{A}_x) & -\frac{\partial \tilde{A}_x}{\partial y} \end{bmatrix} \quad (126)$$

6.5 Power Loss

The total power delivered by the rotating rotor is given by

$$P = \int_{\Gamma_1} \vec{S} \cdot d\Gamma_1 \quad (127)$$

Where the Poynting vector \vec{S} is calculated by

$$\vec{S} = \frac{1}{2} \vec{E} \times \vec{H} = -\frac{1}{2\mu_0} \frac{\partial \vec{A}}{\partial t} \times \vec{B} = -\frac{i\omega_e}{2\mu_0} \vec{A} \times \vec{B} \quad (128)$$

The y direction Poynting vector is calculated by

$$\vec{S} \cdot \hat{y} = \frac{i\omega_e}{2\mu_0} (A_x \bar{B}_z - A_z \bar{B}_x) \quad (129)$$

Using Parseval's theorem, as demonstrated in the previous derivation, the total power can be expressed as

$$P = \text{Re} \left[\frac{i\omega_e}{8\pi^2\mu_0} \int_{-\infty}^{\infty} \int_{-\infty}^{\infty} (\tilde{A}_x \bar{B}_z - \tilde{A}_z \bar{B}_x) d\xi d\zeta \right] \quad (130)$$

The power loss can be calculated as the difference between the total power and the work done on the rotor, expressed as

$$P_{\text{loss}} = P - \vec{F} \cdot \vec{v} = P - F_x v_x \quad (131)$$

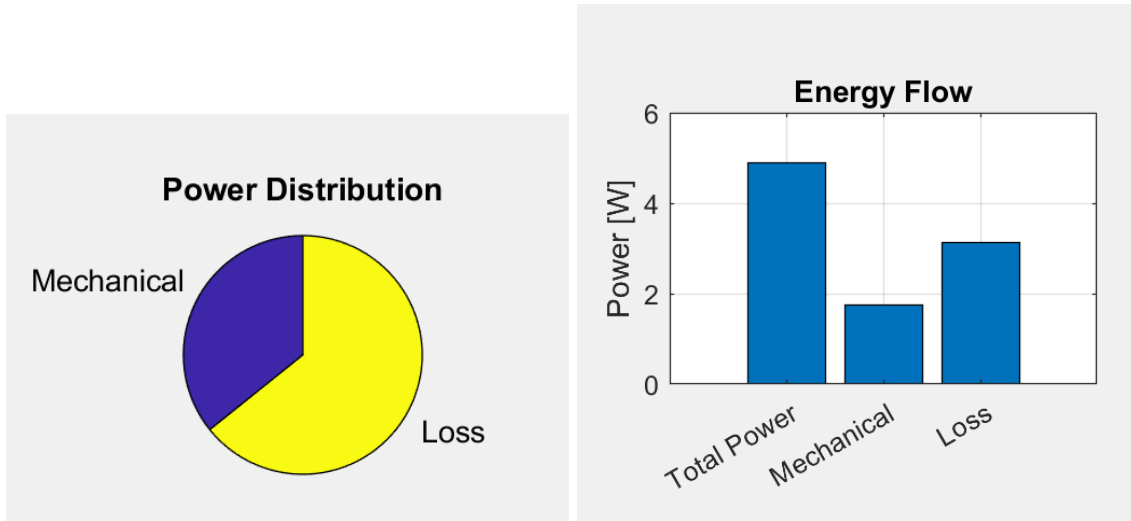


Figure 24: The total power and power loss (a) and (b) respectively

7 Numerical Approximation by Finite Element Method

To validate our general 3-D model, the finite element method (FEM) is adapted to rigorously compare fluctuations between the analytical and numerical results. The finite element method is particularly propitious in handling complex geometries and boundary conditions, which are often present in three-dimensional modelling.

By using FEM, the model is discretized into smaller, manageable elements, allowing for a good approximation of physical properties under various loading conditions.

7.1 Weak Form Formulation

The weak formulation of equation (80) in the region Ω_1 is formulated:

$$\int_{\Omega_1} N_{\Omega_1} \nabla^2 \phi_1 d\Omega_1 = 0 \quad (132)$$

Where N_{Ω_1} is the element shape function defined in the region Ω_1 .

By Green's first identity,

$$N_{\Omega_1} \nabla^2 \phi_1 = N_{\Omega_1} \vec{\nabla} \phi_1 - \vec{\nabla} N_{\Omega_1} \vec{\nabla} \phi_1 \quad (133)$$

Substituting back into the equation (132), the equation becomes [7, 23]

$$\int_{\Gamma_1} N_{\Omega_1} \vec{\nabla} \phi_1 \cdot \hat{n}_c d\Gamma_1 - \int_{\Omega_1} \vec{\nabla} N_{\Omega_1} \cdot \vec{\nabla} \phi_1 d\Omega_1 = 0 \quad (134)$$

The weak form of the magnetic vector potential in equation (77) in the region Ω_2 is given by

$$\int_{\Omega_2} N_{\Omega_2} \nabla^2 \vec{A} d\Omega_2 = \int_{\Omega_2} N_{\Omega_2} \mu_0 \sigma \left(i\omega_e \vec{A} + v_x \frac{\partial \vec{A}}{\partial x} \right) d\Omega_2 \quad (135)$$

Where N_{Ω_2} is the element shape function defined in the region Ω_2 .

By Green's first identity,

$$\begin{aligned} - \int_{\Gamma_1} N_{\Omega_2} \vec{\nabla} \vec{A} \cdot \hat{n}_c d\Gamma_1 + \int_{\Omega_2} \vec{\nabla} N_{\Omega_2} \cdot \vec{\nabla} \vec{A} d\Omega_2 \\ + \mu_0 \sigma \int_{\Omega_2} N_{\Omega_2} \left(i\omega_e \vec{A} + v_x \frac{\partial \vec{A}}{\partial x} \right) d\Omega_2 = 0 \end{aligned} \quad (136)$$

The air and conductive plate regions are interconnected through the application of interface conditions [23, 12], the boundary term vanishes. For each direction, by considering equation (90) (136), we enforce the condition (90) weakly into the equation in each direction, given by [7]

$$\int_{\Gamma_1} N_x \left[\left(\frac{\partial A_x}{\partial x} + A_x \right) \vec{n}_{cx} + \frac{\partial A_x}{\partial y} \vec{n}_{cy} + \frac{\partial A_x}{\partial z} \vec{n}_{cz} \right] d\Gamma_1 = 0 \quad (137)$$

$$\int_{\Gamma_1} N_y \left[\frac{\partial A_y}{\partial x} \vec{n}_{cx} + \left(\frac{\partial A_y}{\partial y} + A_y \right) \vec{n}_{cy} + \frac{\partial A_y}{\partial z} \vec{n}_{cz} \right] d\Gamma_1 = 0 \quad (138)$$

$$\int_{\Gamma_1} N_z \left[\frac{\partial A_z}{\partial x} \vec{n}_{cx} + \frac{\partial A_z}{\partial y} \vec{n}_{cy} + \left(\frac{\partial A_z}{\partial z} + A_z \right) \vec{n}_{cz} \right] d\Gamma_1 = 0 \quad (139)$$

Where \vec{n}_{cx} , \vec{n}_{cy} , \vec{n}_{cz} are the normal vectors of each component and for our problem

$$|\vec{n}_{cy}| = |\hat{n}_c| = 1, \quad |\vec{n}_{cx}| = |\vec{n}_{cz}| = 0 \quad (140)$$

The terms with normal vector \vec{n}_{cx} and \vec{n}_{cz} become trivial. This does the same effect as the gauge transformation we did to ensure that the solution is unique without variation.

Considering $\vec{\nabla} \cdot \vec{A} = 0$ and boundary conditions (83)–(85), the equations can be expressed in terms of the magnetic scalar potential and source field, respectively.

$$\int_{\Gamma_1} N_x \left[\left(A_x - \frac{\partial A_y}{\partial y} - \frac{\partial A_z}{\partial z} \right) \vec{n}_{cx} + \left(\frac{\partial A_y}{\partial x} + \mu_0 \frac{\partial \phi_1}{\partial z} - \vec{B}_z^s \right) \vec{n}_{cy} \right] d\Gamma_1 = 0 \quad (141)$$

$$+ \left(\frac{\partial A_z}{\partial y} - \mu_0 \frac{\partial \phi_1}{\partial y} + \vec{B}_y^s \right) \vec{n}_{cz}$$

$$\int_{\Gamma_1} N_y \left[\left(\frac{\partial A_x}{\partial y} - \mu_0 \frac{\partial \phi_1}{\partial z} + \vec{B}_z^s \right) \vec{n}_{cx} + \left(A_y - \frac{\partial A_x}{\partial x} - \frac{\partial A_z}{\partial z} \right) \vec{n}_{cy} \right] d\Gamma_1 = 0 \quad (142)$$

$$+ \left(\frac{\partial A_z}{\partial y} + \mu_0 \frac{\partial \phi_1}{\partial x} - \vec{B}_x^s \right) \vec{n}_{cz}$$

$$\int_{\Gamma_1} N_z \left[\left(\frac{\partial A_x}{\partial z} + \mu_0 \frac{\partial \phi_1}{\partial y} - \vec{B}_y^s \right) \vec{n}_{cx} + \left(\frac{\partial A_y}{\partial z} + \vec{B}_x^s - \mu_0 \frac{\partial \phi_1}{\partial x} \right) \vec{n}_{cy} \right] d\Gamma_1 = 0 \quad (143)$$

$$+ \left(A_z - \frac{\partial A_x}{\partial x} - \frac{\partial A_y}{\partial y} \right) \vec{n}_{cz}$$

7.2 Upwinding

In this section, we refer to Bird and Lipo (2008) for the weighting procedure utilized in the finite element method. Since equation (77) contains both convection and diffusive contributions, a significant issue exists in the quadrature-upwind scheme, which can experience spurious crosswind effects that compromise the accuracy of the numerical solution. To address this problem, the implementation of the Streamline-Upwind Petrov-Galerkin (SUPG) method is proposed. This approach has been shown to be free from numerical inaccuracies when computing multidimensional problems. SUPG involves selecting a weighting function that differs from the shape function, where the weighting function is defined as

$$W_i = N_i + p_i, \quad \text{where } i \in \{x, y, z\} \quad (144)$$

p_i is defined as

$$\vec{p}_i = \frac{\alpha h}{2} \frac{\vec{v}}{|\vec{v}|} \frac{\partial N_i}{\partial x} \quad (145)$$

Since \vec{v} only has x direction,

$$\vec{p}_i = \frac{\alpha h}{2} \frac{\partial N_i}{\partial x} \frac{v_x}{|\vec{v}|} \hat{x} \quad (146)$$

Where h is the element length of the motion and α is defined as

$$\alpha = \coth(P_e) - \frac{1}{P_e} \quad (147)$$

The Peclet number serves as a crucial parameter for modelling spurious numerical oscillatory behaviour in simulations and is defined as [10]

$$P_e = \frac{\mu_0 \sigma v h}{2} \quad (148)$$

The application of the weighting function is essential in the presence of a convective velocity term. This means that the modified weighting function is implemented exclusively for the volume region terms [7].

Considering all the above, the weak formation of equation (136) for each direction can be expressed as

$$-\int_{\Gamma_1} N_i \vec{\nabla} \vec{A}_i \cdot \hat{n}_c d\Gamma_1 + \int_{\Omega_2} \vec{\nabla} N_i \cdot \vec{\nabla} \vec{A}_i d\Omega_2$$

$$+ \mu_0 \sigma \int_{\Omega_2} W_i \left(i\omega_e \vec{A}_i + v_x \frac{\partial \vec{A}_i}{\partial x} \right) d\Omega_2 - \int_{\Omega_2} \vec{p}_i \cdot \nabla^2 \vec{A}_i d\Omega_2 = 0$$

$$\text{for } i \in \{x, y, z\} \quad (149)$$

A finite element method expression is obtained that allows numerical solving of the parameters.

7.3 Result Plot

Below shows the FEM result for the magnetic source field.

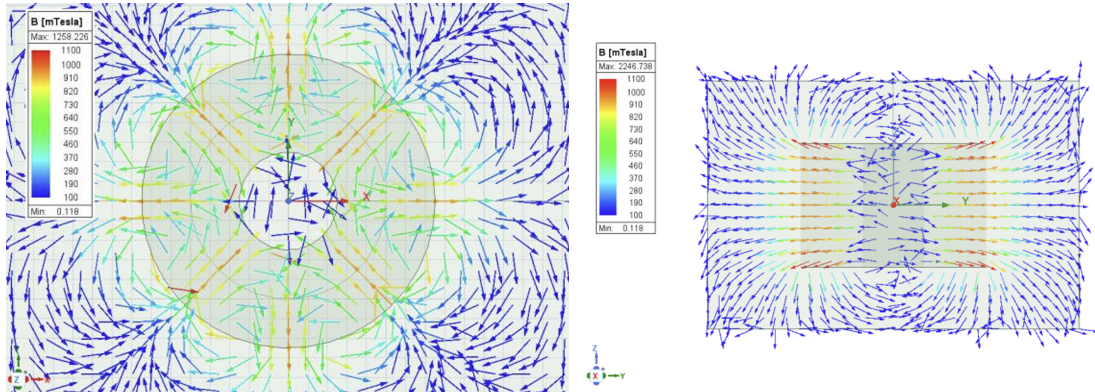


Figure 25: Magnetic field vector for the external rotor on xy plane and yz plane respectively

The FEM result for the rotor travelling and rotating on an aluminium plate is shown below.

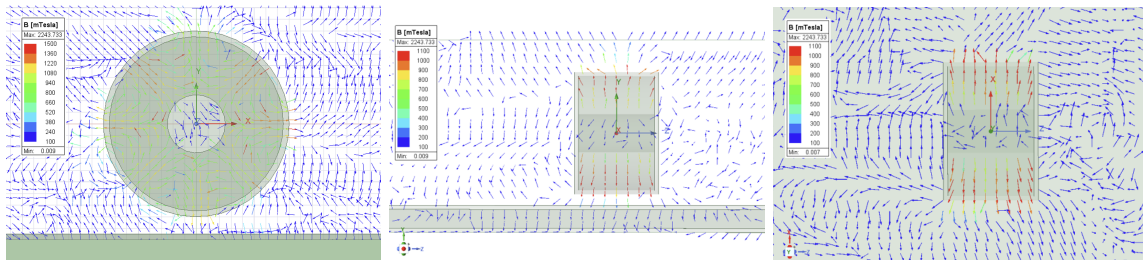


Figure 26: Magnetic field vector for xy, yz and xz plane respectively

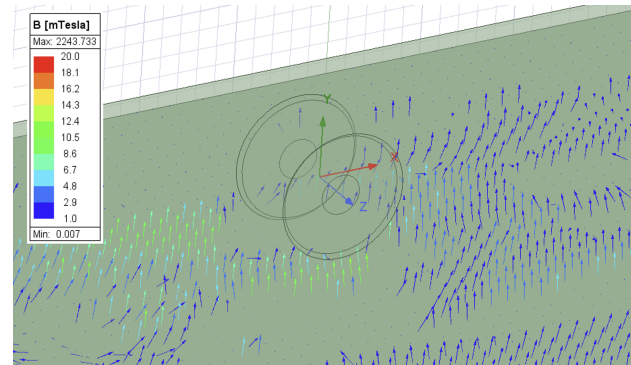


Figure 27: Magnetic field reaction of the aluminium plate

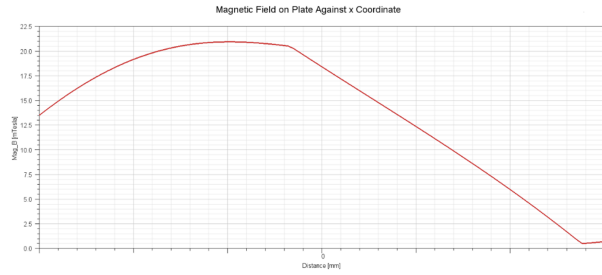


Figure 28: Magnetic field magnitude on the plate against the x-coordinate

8 Model Comparison

8.1 Source Field Comparison

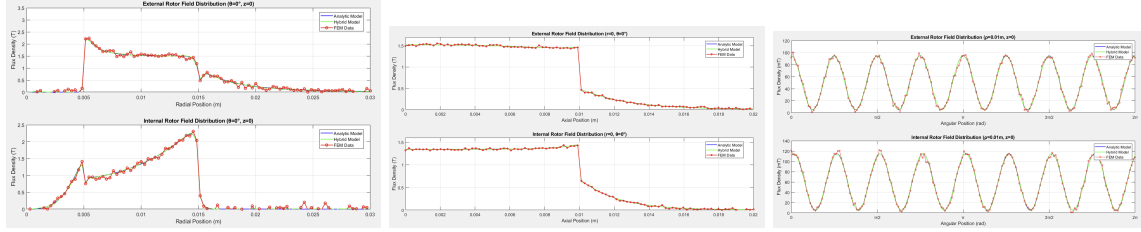


Figure 29: Magnitude of magnetic field comparisons between 3 models

8.2 Plate Components Comparison

The result shows that the forces are oscillating in a period of $T = \pi/P$, aligning with the finding in section 3. The thrust force acts as a cosine function while the levitation force acts as a sine function. After comparison, we can observe that there is a strong agreement between the 2 models.

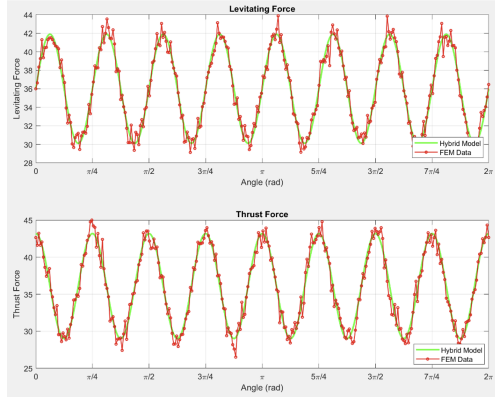


Figure 30: Magnitude of thrust force and levitation force comparison between 2 models

9 Conclusion

9.1 Research Result

Our model contributes to a rigorous and complete 3D analysis of the field and force components of the Halbach rotor.

For the source field, by using the magnetic charge model, the exact solution of the 3D source field of Halbach rotor is found, presented in equation (8). The solution can be further decomposed by using the orthogonal greedy algorithm, presented in section 4, to numerically analyse its eigenvalues and dependencies. This approach significantly simplifies the 3D expression and has higher utility over pure analytical and numerical models, as it can be directly used in different analyses.

For the analysis on the Halbach rotor on a conductive plate, we derived a force equation based on the thin sheet approximation, denoted as equation (31). To further address the problem, a comprehensive analysis is taken in sections 5 and 6, deriving a force equation as well as the induced eddy current. These analysis serves as a foundation for complex 3D analysis in the future.

9.2 Future Analysis

- **Rotor Design:** The rotor design in our model comprises only magnets, lacking specific components like a soft iron shell. Additionally, we assume that the magnets are tightly packed with no air gaps, which does not reflect real-world rotors. Future work should include a field analysis of various rotor shell designs.
- **Variation of Parameters:** We employ a fixed parameter for the numerical analysis. It is advisable to include comparisons among different parameters. This analysis is crucial for optimizing different components on different occasions.
- **Comparison with Traditional Rotor:** A comparison with traditional rotors can reveal the extent of improvements achieved when magnets are arranged in a Halbach array, such as increased magnetic field strength and efficiency. This future analysis can let us have a better understanding of the advantages of using a Halbach array in rotor design.

References

- [1] Three-dimensional steady state and transient eddy current modeling, 1985. URL <https://www.proquest.com/openview/e368715b49fdabfddc44403c7d117241/1>.
- [2] Dynamic suspension modeling of an eddy-current device: An application to maglev, 2007. URL <https://www.proquest.com/openview/4d11489ef40d45aa979755ca0d65a7cd/1>.
- [3] Theory 3: Magnetic levitation solution, 2021. URL https://apho.olimpicos.net/pdf/APhO_2021_S3.pdf.
- [4] General 3d analytical method for eddy-current coupling with halbach magnet arrays based on magnetic scalar potential and h-functions, 2021. URL <https://www.mdpi.com/1996-1073/14/24/8458>.
- [5] Electrodynamic wheel magnetic levitation in 2d, 2023. URL <https://www.comsol.com/model/electrodynamic-wheel-magnetic-levitation-in-2d-44871>.
- [6] H. Abdi. Singular value decomposition (svd) and generalized singular value decomposition. In *Encyclopedia of Measurement and Statistics*, pages 907–912. Sage, 2007.
- [7] J. Bird and T. A. Lipo. A 3-d magnetic charge finite-element model of an electrodynamic wheel. *IEEE Transactions on Magnetics*, 44(2):253–265, feb 2008. doi: 10.1109/TMAG.2007.911597.
- [8] J. Bird and T. A. Lipo. Modeling the 3-d rotational and translational motion of a halbach rotor above a split-sheet guideway. *IEEE Transactions on Magnetics*, 45(9):3233–3242, sep 2009. doi: 10.1109/TMAG.2009.2021160.
- [9] D. Brown, B. Ma, and Z. Chen. Developments in the processing and properties of ndfeb-type permanent magnets. *Journal of Magnetism and Magnetic Materials*, 248(3):432–440, 2002. doi: 10.1016/S0304-8853(02)00334-7.
- [10] E. K. C. Chan and S. Williamson. Factors influencing the need for upwinding in two-dimensional field calculation. *IEEE Transactions on Magnetics*, 28(2):1611–1614, mar 1992. doi: 10.1109/20.124008.
- [11] K. Davey. Optimization shows halbach arrays to be non-ideal for induction devices. *IEEE Transactions on Magnetics*, 36(4):1035–1038, jul 2000. doi: 10.1109/20.877618.
- [12] C. Emson and J. Simkin. An optimal method for 3-d eddy currents. *IEEE Transactions on Magnetics*, 19(6):2450–2452, nov 1983. doi: 10.1109/TMAG.1983.1062910.
- [13] S. E. Gay and M. Ehsani. Parametric analysis of eddy-current brake performance by 3-d finite-element analysis. *IEEE Transactions on Magnetics*, 42(2):319–328, feb 2006. doi: 10.1109/TMAG.2005.860782.
- [14] G. H. Golub, P. C. Hansen, and D. P. O’Leary. Tikhonov regularization and total least squares. *SIAM Journal on Matrix Analysis and Applications*, 21(1):185–194, 1999.
- [15] D. J. Griffiths. *Introduction to Electrodynamics*. Cambridge University Press, 4th edition, 2021.
- [16] C. W. Groetsch. *The Theory of Tikhonov Regularization for Fredholm Equations of the First Kind*. Pitman Advanced Publishing Program, Boston, 1984.
- [17] J. D. Jackson. *Classical Electrodynamics*. Wiley, 3rd edition, 1999.
- [18] A. K. Jha. *Design of Halbach Permanent Magnet External-Rotor Machine with Reuse & Recycle Magnet Concepts for Automotive Applications*. PhD thesis, Université Grenoble Alpes, Grenoble, France, 2019. URL <https://tel.archives-ouvertes.fr/tel-02295220v1>.
- [19] J. C. Maxwell. On the induction of electric currents in an infinite plane sheet of uniform conductivity. *Proceedings of the Royal Society of London*, 20(130–138):159–168, 1871. doi: 10.1098/rspl.1871.0038.

- [20] K. J. Meessen. *Electromagnetic fields and interactions in 3D cylindrical structures: modeling and application*. Technische Universiteit Eindhoven, Eindhoven, 2012.
- [21] P. Oswald. Greedy algorithms and best m-term approximation with respect to biorthogonal systems. *Journal of Fourier Analysis and Applications*, 7(4):325–341, 2001.
- [22] N. Paudel, S. Paul, and J. Z. Bird. General 2d steady-state force and power equations for a traveling time-varying magnetic source above a conductive plate. *Progress In Electromagnetics Research B*, 43: 255–277, 2012. doi: 10.2528/PIERB12072414.
- [23] R. Pillsbury. A three dimensional eddy current formulation using two potentials: The magnetic vector potential and total magnetic scalar potential. *IEEE Transactions on Magnetics*, 19(6):2284–2287, nov 1983. doi: 10.1109/TMAG.1983.1062819.
- [24] S. K. Sharan. Eddy current damping in structures. *The Shock and Vibration Digest*, 36(6):469–478, 2004. doi: 10.1177/0583102404048517.
- [25] M.-S. Sim and J.-S. Ro. Semi-analytical modeling and analysis of halbach array. *Energies*, 13(5):1252, 2020. doi: 10.3390/en13051252.
- [26] R. K. Srivastava and S. Kumar. An alternative approach for calculation of braking force of an eddy-current brake. *IEEE Transactions on Magnetics*, 45(1):150–154, jan 2009. doi: 10.1109/TMAG.2008.2006993.
- [27] G. Strang. *Linear Algebra and Learning from Data*, volume 4. Wellesley-Cambridge Press, 2019.
- [28] G. Strang. *Introduction to Linear Algebra*. Wellesley-Cambridge Press, 5th edition, 2022.
- [29] M. T. Thompson. Practical issues in the use of ndfeb permanent magnets in maglev, motors, bearings, and eddy current brakes. *Proceedings of the IEEE*, 97(11):1758–1767, nov 2009. doi: 10.1109/JPROC.2009.2030231.
- [30] J. A. Tropp. Greed is good: Algorithmic results for sparse approximation. *IEEE Transactions on Information Theory*, 50(10):2231–2242, 2004.
- [31] Z. P. Xia, Z. Q. Zhu, and D. Howe. Analytical magnetic field analysis of halbach magnetized permanent-magnet machines. *IEEE Transactions on Magnetics*, 40(4):1864–1872, jul 2004. doi: 10.1109/TMAG.2004.828933.
- [32] O. Zienkiewicz, J. Lyness, and D. Owen. Three-dimensional magnetic field determination using a scalar potential—a finite element solution. *IEEE Transactions on Magnetics*, 13(5):1649–1656, sep 1977. doi: 10.1109/TMAG.1977.1059650.

A1 Green's Function for the Laplace Operator

The Laplace operator in cylindrical coordinates has the form

$$\frac{1}{\rho} \frac{\partial}{\partial \rho} \left(\rho \frac{\partial \phi}{\partial \rho} \right) + \frac{1}{\rho^2} \frac{\partial^2 \phi}{\partial \theta^2} + \frac{\partial^2 \phi}{\partial z^2} = -f(\rho, \theta) \quad (150)$$

Where the $-f(\rho, \theta)$ accounts for the source term.

The free-space Green's function can be constructed through

$$\begin{aligned} \frac{1}{\rho} \frac{\partial}{\partial \rho} \left(\rho \frac{\partial g(\rho, \theta, z | \rho', \theta', z')}{\partial \rho} \right) + \frac{1}{\rho^2} \frac{\partial^2 g(\rho, \theta, z | \rho', \theta', z')}{\partial \theta^2} + \frac{\partial^2 g(\rho, \theta, z | \rho', \theta', z')}{\partial z^2} \\ = -\frac{\delta(\rho - \rho') \delta(\theta - \theta') \delta(z - z')}{\rho} \end{aligned} \quad (151)$$

Where the parameters are limited by

$$0 \leq \rho, \rho' < \infty, \quad 0 \leq \theta, \theta' \leq 2\pi, \quad -\infty \leq z, z' < \infty \quad (152)$$

From Jackson and Fox (1999),

$$\delta(\theta - \theta') = \frac{1}{2\pi} + \frac{1}{\pi} \sum_{n=1}^{\infty} \cos[n(\theta - \theta')] = \frac{1}{2\pi} \sum_{n=-\infty}^{\infty} \cos[n(\theta - \theta')] \quad (153)$$

The form of Green's function can be inferred based on equation (153).

$$g(\rho, \theta, z | \rho', \theta', z') = \sum_{n=-\infty}^{\infty} g_n(\rho, z | \rho', z') \cos[n(\theta - \theta')] \quad (154)$$

By substituting (154) in (151), an expression for each mode n is obtained:

$$\frac{1}{\rho} \frac{\partial}{\partial \rho} \left(\rho \frac{\partial g_n}{\partial \rho} \right) - \frac{n^2}{\rho^2} g_n + \frac{\partial^2 g_n}{\partial z^2} = -\frac{\delta(\rho - \rho') \delta(z - z')}{2\pi\rho} \quad (155)$$

By taking the Hankel transform with a constant k on both sides, the LHS becomes

$$\int_0^\infty \left[\frac{1}{\rho} \frac{\partial}{\partial \rho} \left(\rho \frac{\partial g_n}{\partial \rho} \right) - \frac{n^2}{\rho^2} g_n + \frac{\partial^2 g_n}{\partial z^2} \right] \rho J_n(k\rho) d\rho \quad (156)$$

Considering

$$\begin{aligned} \frac{1}{\rho} \frac{\partial}{\partial \rho} \left(\rho \frac{\partial J_n(k\rho)}{\partial \rho} \right) + \left(k^2 - \frac{n^2}{\rho^2} \right) J_n(k\rho) \\ = k^2 J_n''(k\rho) + \frac{k}{\rho} J_n'(k\rho) + \left(k^2 - \frac{n^2}{\rho^2} \right) J_n(k\rho) = 0 \end{aligned} \quad (157)$$

The terms excluding the axial term in equation (156) can be simplified by performing integration by parts twice:

$$\begin{aligned} & \int_0^\infty \left[\frac{\partial^2 g_n}{\partial \rho^2} + \frac{1}{\rho} \frac{\partial g_n}{\partial \rho} - \frac{n^2}{\rho^2} g_n \right] \rho J_n(k\rho) d\rho \\ &= \left[\rho J_n(k\rho) \frac{\partial g_n}{\partial \rho} \right]_0^\infty - \int_0^\infty k \frac{\partial g_n}{\partial \rho} \rho J_n'(k\rho) d\rho - \int_0^\infty \frac{n^2}{\rho} g_n J_n(k\rho) d\rho \\ &= -k [\rho J_n'(k\rho) g_n]_0^\infty + \int_0^\infty g_n \left[k^2 \rho J_n'' + k J_n'(k\rho) - \frac{n^2}{\rho} J_n(k\rho) \right] d\rho \\ &= -k^2 \int_0^\infty g_n \rho J_n(k\rho) d\rho = -k^2 G_n \end{aligned} \quad (158)$$

Where G_n is the Hankel transformed Green's function.

The RHS of the equation can be simplified by the property of the Dirac delta function:

$$-\int_0^\infty \frac{\delta(\rho - \rho')\delta(z - z')}{2\pi\rho} \rho J_n(k\rho) d\rho = -\frac{1}{2\pi} J_n(k\rho') \delta(z - z') \quad (159)$$

By substituting (158) and (159) into (155),

$$\frac{\partial^2 G_n}{\partial z^2} - k^2 G_n = -\frac{1}{2\pi} J_n(k\rho') \delta(z - z') \quad (160)$$

A solution for G_n is obtained:

$$G_n(k, z|\rho', z') = \frac{1}{4\pi k} J_n(k\rho') e^{-k|z-z'|} \quad (161)$$

The original Green's function can be obtained by inverse Hankel transform.

$$g(\rho, \theta, z|\rho', \theta', z') = \frac{1}{4\pi} \int_0^\infty \sum_{n=-\infty}^{\infty} J_n(k\rho) J_n(k\rho') e^{-k|z-z'|} \cos[n(\theta - \theta')] dk \quad (162)$$

By the addition theorem of Bessel functions, from Davis and Watson (1944b),

$$J_0 \left[k \sqrt{\rho^2 + \rho'^2 - 2\rho\rho' \cos(\theta - \theta')} \right] = \sum_{n=-\infty}^{\infty} J_n(k\rho) J_n(k\rho') \cos[n(\theta - \theta')] \quad (163)$$

The Green's function is now expressed as

$$g(\rho, \theta, z|\rho', \theta', z') = \frac{1}{4\pi} \int_0^\infty e^{-k|z-z'|} J_0(kR) dk \quad (164)$$

Where $R = \sqrt{\rho^2 + \rho'^2 - 2\rho\rho' \cos(\theta - \theta')}$.

By the definition of Bessel function of the first kind $J_0(kR) = \frac{1}{\pi} \int_0^{2\pi} \cos(kR \sin \varphi) d\varphi$ and the Laplace transformation formula $\int_0^\infty e^{-ak} \cos(bk) dk = \frac{a}{a^2 + b^2}$, the final form of the expression is given by

$$\begin{aligned} g(\rho, \theta, z|\rho', \theta', z') &= \frac{1}{4\pi^2} \int_0^{2\pi} \frac{|z - z'|}{(z - z')^2 + R^2 \sin^2 \varphi} d\varphi \\ &= \frac{1}{4\pi} [\rho^2 + \rho'^2 - 2\rho\rho' \cos(\theta - \theta') + (z - z')^2]^{-1/2} \end{aligned} \quad (165)$$

A2 Integral Transformation of Derivative Functions

The Fourier transformation of a function $f(x)$ is given by

$$\tilde{f}(\xi) = \int_{-\infty}^{\infty} f(x) e^{i\xi x} dx \quad (166)$$

The derivative transformation is given by

$$\begin{aligned} \int_{-\infty}^{\infty} \frac{\partial f(x)}{\partial x} e^{i\xi x} dx &= \underbrace{[f(x) e^{i\xi x}]_{-\infty}^{\infty}}_{=0} - i\xi \int_{-\infty}^{\infty} f(x) e^{i\xi x} dx \\ &= -i\xi \tilde{f}(\xi) \end{aligned} \quad (167)$$

The contribution of $f(x)$ is assumed to vanish at infinity. By utilizing (167), the derivative transformation is generalized by

$$\int_{-\infty}^{\infty} \frac{\partial^n f(x)}{\partial x^n} e^{i\xi x} dx = (-i\xi)^n \tilde{f}(\xi), \quad n \in \mathbb{Z}^+ \quad (168)$$

A3 Details and Results of Orthogonal Greedy Algorithm

Below displays the MATLAB code used for Ω_{IV} external rotor.

```

1 clc; clearvars; close all;
2
3 % Parameters
4 MO = 1e6; % Magnetisation amplitude [A/m]
5 P = 4; % Pole-pair number (integer      1)
6 Ri = 0.005; % Inner radius [m]
7 Ro = 0.015; % Outer radius [m]
8 Wr = 0.02; % Magnet height (total) [m]
9 N_r = 50; % Radial collocation points
10 N_z = 50; % Axial collocation points
11 theta0 = 0; % Azimuthal angle
12 k_min = 1e-10; % Minimum k search bound [1/m]
13 k_max = 5000; % Maximum k search bound [1/m]
14 MAX_TERMS = 200; % Maximum number of modes
15 TARGET_REL_ERR = 0.01; % 1% target RMS error
16 ABS_TOL = 1e-8; % Integral absolute tolerance
17 REL_TOL = 1e-4; % Integral relative tolerance
18 ORTHO_TOL = 1e-4; % Looser orthogonality tolerance
19 MIN_NORM = 1e-6; % Looser minimum vector norm threshold
20 MAX_TRIALS_PER_TERM = 100; % Trials per term
21
22 % Create collocation grid ( , z) for region IV
23 rho_vec = linspace(Ro, Ro*1.5, N_r);
24 z_vec = linspace(0, Wr/2, N_z);
25 [RR, ZZ] = ndgrid(rho_vec, z_vec);
26 ntotal = numel(RR);
27
28 % Run only for external rotor
29 rotor_type = 'external';
30 fprintf('\n===== Processing %s rotor configuration (Region IV) =====\n', rotor_type);
31
32 % Compute exact potential _exact on grid
33 fprintf('Evaluating exact potential on %d x %d grid...\n', N_r, N_z);
34 phi_exact = zeros(ntotal, 1);
35 volume_factor = (1 - P); % External rotor factor
36
37 warnState = warning('off', 'all');
38 for idx = 1:ntotal
39     rho = RR(idx);
40     z = ZZ(idx);
41     phi_val = computePoint(rho, z, theta0, Ri, Ro, Wr, P, MO, volume_factor, ABS_TOL,
42     REL_TOL);
43     phi_exact(idx) = phi_val;
44 end
45 warning(warnState);
46
47 fprintf('Exact potential computed.\n');
48 norm_exact = norm(phi_exact);
49 fprintf('Exact potential RMS norm: %.4g\n', norm_exact);
50
51 % Scale for numerical stability
52 potential_scale = norm_exact;
53 phi_exact_scaled = phi_exact / potential_scale;
54
55 % Initialize variables
56 k_list = [];
57 type_list = [];
58 C_list_scaled = [];
59 B_normalized = [];
60 err_hist = [];
61 current_err = 1.0;
62 n_terms = 0;
63 fprintf('\nStarting adaptive greedy basis construction...\n');
```

```

64
65 for n = 1:MAX_TERMS
66 % Compute current residual
67 if isempty(B_normalized)
68     r0 = phi_exact_scaled;
69 else
70     % Use least squares with regularization
71     [U, S, V] = svd(B_normalized, 'econ');
72     s = diag(S);
73     rank = sum(s > 1e-12 * max(s));
74     if rank > 0
75         lambda = 1e-8 * max(s);
76         s_inv = diag(s(1:rank) ./ (s(1:rank).^2 + lambda^2));
77         C_current = V(:, 1:rank) * s_inv * (U(:, 1:rank)' * phi_exact_scaled);
78         r0 = phi_exact_scaled - B_normalized * C_current;
79     else
80         r0 = phi_exact_scaled;
81     end
82 end
83
84 norm_r0 = norm(r0);
85 if n_terms == 0
86     fprintf('Initial residual norm: %.6f\n', norm_r0);
87 end
88
89 % Adaptive k-space scanning based on current error
90 if current_err > 0.5
91     % High error - scan broadly
92     k_scans = {
93         logspace(log10(k_min), log10(1e-2), 100),
94         logspace(log10(1e-2), log10(1), 200),
95         logspace(log10(1), log10(100), 300),
96         logspace(log10(100), log10(k_max), 200)
97     };
98 elseif current_err > 0.1
99     % Medium error - focus on medium frequencies
100    k_scans = {
101        logspace(log10(1e-3), log10(10), 400),
102        logspace(log10(10), log10(500), 400)
103    };
104 else
105     % Low error - refine existing frequencies
106     if ~isempty(k_list)
107         % Focus around existing k values
108         k_centers = unique(k_list);
109         k_scans = {};
110         for kc = k_centers
111             if kc > 0
112                 lb = max(k_min, 0.1 * kc);
113                 ub = min(k_max, 10 * kc);
114                 k_scans{end+1} = logspace(log10(lb), log10(ub), 200);
115             end
116         end
117         % Also include some random exploration
118         k_scans{end+1} = logspace(log10(k_min), log10(k_max), 300);
119     else
120         k_scans = {logspace(log10(k_min), log10(k_max), 500)};
121     end
122 end
123
124 best_candidate = [];
125 best_candidate_err = inf;
126
127 fprintf('Term %d: Scanning %d frequency ranges...\n', n, length(k_scans));
128
129 for scan_idx = 1:length(k_scans)
130     k_scan = k_scans{scan_idx};

```

```

132     for type_idx = 1:2
133         for k_idx = 1:length(k_scan)
134             k0 = k_scan(k_idx);
135
136             % Skip if this k-type combination already exists
137             if any(k_list == k0 & type_list == type_idx)
138                 continue;
139             end
140
141             v = basisVectorIV(k0, type_idx, RR, ZZ, P);
142             v_norm = norm(v);
143
144             if v_norm < MIN_NORM
145                 continue;
146             end
147
148             v_normalized = v / v_norm;
149
150             % Check orthogonality with current basis
151             if ~isempty(B_normalized)
152                 proj = B_normalized' * v_normalized;
153                 if abs(proj) > 0.99 % Nearly parallel to existing basis
154                     continue;
155                 end
156             end
157
158             % Simple projection test - how much does this reduce residual?
159             proj_r = dot(r0, v_normalized);
160             candidate_err = sqrt(max(0, norm_r0^2 - proj_r^2)) / norm(phi_exact_scaled);
161
162             if candidate_err < best_candidate_err
163                 best_candidate_err = candidate_err;
164                 best_candidate = struct('k', k0, 'type', type_idx, 'v', v, 'v_norm',
165                                         v_norm);
166             end
167         end
168     end
169
170     if isempty(best_candidate)
171         fprintf('No candidate found in scan. Trying emergency measures...\n');
172
173     % Emergency: try random k values
174     emergency_ks = [logspace(log10(k_min), log10(k_max), 1000), ...
175                     rand(1, 500) * (k_max - k_min) + k_min];
176
177     for k0 = emergency_ks
178         for type_idx = 1:2
179             v = basisVectorIV(k0, type_idx, RR, ZZ, P);
180             v_norm = norm(v);
181             if v_norm > MIN_NORM
182                 v_normalized = v / v_norm;
183                 proj_r = dot(r0, v_normalized);
184                 candidate_err = sqrt(max(0, norm_r0^2 - proj_r^2)) / norm(
phi_exact_scaled);
185
186                 if candidate_err < best_candidate_err
187                     best_candidate_err = candidate_err;
188                     best_candidate = struct('k', k0, 'type', type_idx, 'v', v, 'v_norm',
189                                         v_norm);
190                 end
191             end
192         end
193     end
194
195     if isempty(best_candidate)
196         fprintf('No valid candidate found after emergency scan. Stopping.\n');

```

```

197     break;
198 end
199
200 % Add the best candidate
201 k_opt = best_candidate.k;
202 type_opt = best_candidate.type;
203 v_opt_normalized = best_candidate.v / best_candidate.v_norm;
204
205 B_temp = [B_normalized, v_opt_normalized];
206
207 % Solve for new coefficients
208 [U, S, V] = svd(B_temp, 'econ');
209 s = diag(S);
210 rank = sum(s > 1e-12 * max(s));
211
212 if rank > 0
213     lambda = 1e-8 * max(s);
214     s_inv = diag(s(1:rank) ./ (s(1:rank).^2 + lambda^2));
215     C_temp = V(:, 1:rank) * s_inv * (U(:, 1:rank))' * phi_exact_scaled;
216     residual = phi_exact_scaled - B_temp * C_temp;
217     current_err_candidate = norm(residual);
218 else
219     C_temp = [];
220     current_err_candidate = 1.0;
221 end
222
223 % Always accept if it improves error
224 if current_err_candidate <= current_err || n_terms < 5 % Force first 5 terms
225     k_list(end+1) = k_opt;
226     type_list(end+1) = type_opt;
227     B_normalized = B_temp;
228     C_list_scaled = C_temp;
229     prev_err = current_err;
230     current_err = current_err_candidate;
231     err_hist(end+1) = current_err;
232     n_terms = n_terms + 1;
233
234     error_reduction = prev_err - current_err;
235     fprintf('Term %d: type=%d, k_n=% .6f, RelErr=% .6f%%,    =% .6f%%, max|C|=% .2e\n', ...
236             n_terms, type_opt, k_opt, 100*current_err, 100*error_reduction, max(abs(C_temp))
237 );
238
239 % Check convergence
240 if current_err < TARGET_REL_ERR
241     fprintf('\n      TARGET ACHIEVED: Error (%.6f%%) < target (%.4f%%) with %d terms
242 !\n', ...
243             100*current_err, 100*TARGET_REL_ERR, n_terms);
244     break;
245 end
246
247 % Force at least 10 terms before considering stopping
248 if n_terms >= 10 && error_reduction < 1e-6
249     fprintf('Minimal improvement. Stopping.\n');
250     break;
251 end
252
253 else
254     fprintf('Candidate rejected (no improvement). Continuing search...\n');
255 end
256
257 % Don't stop early - keep going until we have reasonable terms
258 if n_terms >= 50 && current_err < 0.05 % Good enough
259     fprintf('Reasonable accuracy achieved with %d terms. Stopping.\n', n_terms);
260     break;
261 end
262
263 % Transform coefficients back to original space
264 fprintf('\nComputing final coefficients...\n');

```

```

263 C_list_final = zeros(size(C_list_scaled));
264
265 for i = 1:length(k_list)
266     basis_func = basisVectorIV(k_list(i), type_list(i), RR, ZZ, P);
267     basis_norm = norm(basis_func);
268     if basis_norm > 0
269         C_list_final(i) = C_list_scaled(i) * potential_scale / basis_norm;
270     else
271         C_list_final(i) = 0;
272     end
273 end
274 C_list = C_list_final;
275
276 % Output results
277 fprintf('\n%*s Rotor (Region IV): Results\n', upper(rotor_type));
278 fprintf('%-6s %-12s %-15s %-15s\n', 'Index', 'k_n [1/m]', 'Bessel Type', 'C(n)');
279 fprintf('-----\n');
280 for i = 1:length(k_list)
281     bessel_type = {'J_P', 'Y_P'};
282     fprintf('%-6d %-12.6f %-15s %-15.6g\n', i, k_list(i), bessel_type{type_list(i)}, C_list(i));
283 end
284 fprintf('-----\n');
285 fprintf('Final RMS error: %.6f%\n', 100*current_err);
286 fprintf('Number of terms: %d\n', n_terms);
287
288 % Compute verification
289 fprintf('\nComputing verification...\n');
290 phi_approx = zeros(size(phi_exact));
291 for i = 1:length(k_list)
292     basis_func = basisVectorIV(k_list(i), type_list(i), RR, ZZ, P);
293     phi_approx = phi_approx + C_list(i) * basis_func;
294 end
295
296 abs_error = phi_exact - phi_approx;
297 rel_error = abs_error ./ (abs(phi_exact) + eps);
298 rms_abs_error = sqrt(mean(abs_error.^2));
299 rms_rel_error = sqrt(mean(rel_error.^2));
300
301 fprintf('\n==== VERIFICATION ====\n');
302 fprintf('RMS Absolute Error: %.6e\n', rms_abs_error);
303 fprintf('RMS Relative Error: %.6f%\n', 100*rms_rel_error);
304 fprintf('Maximum Absolute Error: %.6e\n', max(abs(abs_error)));
305 fprintf('Maximum Relative Error: %.6f%\n', 100*max(abs(rel_error)));
306
307 % Plot results
308 phi_exact_grid = reshape(phi_exact, size(RR));
309 phi_approx_grid = reshape(phi_approx, size(RR));
310 abs_error_grid = reshape(abs_error, size(RR));
311 rel_error_grid = reshape(rel_error, size(RR));
312
313 plotResults(RR, ZZ, phi_exact_grid, phi_approx_grid, abs_error_grid, rel_error_grid, ...
314             k_list, type_list, C_list, err_hist, Ri, Ro, Wr, rotor_type);
315
316 % Save results
317 eigenvalues = k_list;
318 basis_types = type_list;
319 coefficients = C_list;
320
321 save('external_rotor_results.mat', 'eigenvalues', 'basis_types', 'coefficients', ...
322       'rotor_type', 'P', 'Ri', 'Ro', 'Wr', 'phi_exact', 'phi_approx', ...
323       'rms_abs_error', 'rms_rel_error', 'TARGET_REL_ERR');
324
325 fprintf('Results saved to external_rotor_results.mat\n');
326
327 %% Helper Functions
328 function phi = computePoint(rho, z, theta, Ri, Ro, Wr, P, M0, volume_factor, abs_tol, ...
    rel_tol)

```

```

329 phi = 0;
330 eps_dist = 1e-12;
331
332 try
333     intVol = @(rp, tp, zp) cos(P*tp) ./ max(sqrt(rho^2 + rp.^2 - 2*rho*rp.*cos(theta-tp) + (z-zp).^2), eps_dist);
334     intRi = @(tp, zp) cos(P*tp) ./ max(sqrt(rho^2 + Ri^2 - 2*rho*Ri*cos(theta-tp) + (z-zp).^2), eps_dist);
335     intRo = @(tp, zp) cos(P*tp) ./ max(sqrt(rho^2 + Ro^2 - 2*rho*Ro*cos(theta-tp) + (z-zp).^2), eps_dist);
336
337     I1 = integral3(intVol, Ri, Ro, 0, 2*pi, -Wr/2, Wr/2, 'AbsTol', abs_tol, 'RelTol', rel_tol);
338     I2 = integral2(intRi, 0, 2*pi, -Wr/2, Wr/2, 'AbsTol', abs_tol, 'RelTol', rel_tol);
339     I3 = integral2(intRo, 0, 2*pi, -Wr/2, Wr/2, 'AbsTol', abs_tol, 'RelTol', rel_tol);
340
341     phi = M0/(4*pi) * (volume_factor * I1 - Ri*I2 + Ro*I3);
342
343 catch
344     phi = 0;
345 end
346 end
347
348 function v = basisVectorIV(k, type, RR, ZZ, P)
349 rho_vals = RR(:);
350 z_vals = ZZ(:);
351 k = abs(k);
352
353 if k > 1e4
354     v = zeros(size(rho_vals));
355     return;
356 end
357
358 switch type
359     case 1
360         v = exp(-k * abs(z_vals)) .* besselj(P, k * rho_vals);
361     case 2
362         valid = rho_vals > 1e-12;
363         v = zeros(size(rho_vals));
364         v(valid) = exp(-k * abs(z_vals(valid))) .* bessely(P, k * rho_vals(valid));
365         v(isinf(v) | isnan(v)) = 0;
366 end
367 end
368
369 function plotResults(RR, ZZ, phi_exact, phi_approx, abs_error, rel_error, ...
370                      k_list, type_list, C_list, err_hist, Ri, Ro, Wr, rotor_type)
371
372     font_size = 12;
373
374     % 1. Potential Comparison
375     fig1 = figure('Position', [100, 100, 1200, 800]);
376     sgttitle(sprintf('%s Rotor - Results', upper(rotor_type)), 'FontSize', font_size+2);
377
378     subplot(2,3,1);
379     contourf(RR, ZZ, phi_exact, 30, 'LineColor', 'none');
380     colorbar; axis equal tight;
381     title('Exact Potential');
382     xlabel('\rho [m]'); ylabel('z [m]');
383
384     subplot(2,3,2);
385     contourf(RR, ZZ, phi_approx, 30, 'LineColor', 'none');
386     colorbar; axis equal tight;
387     title('Approximate Potential');
388     xlabel('\rho [m]'); ylabel('z [m]');
389
390     subplot(2,3,3);
391     contourf(RR, ZZ, phi_exact - phi_approx, 30, 'LineColor', 'none');
392     colorbar; axis equal tight;

```

```

393 title('Difference');
394 xlabel('\rho [m]'); ylabel('z [m]');
395
396 subplot(2,3,4);
397 contourf(RR, ZZ, abs_error, 30, 'LineColor', 'none');
398 colorbar; axis equal tight;
399 title('Absolute Error');
400 xlabel('\rho [m]'); ylabel('z [m]');
401
402 subplot(2,3,5);
403 contourf(RR, ZZ, rel_error * 100, 30, 'LineColor', 'none');
404 colorbar; axis equal tight;
405 title('Relative Error (%)');
406 xlabel('\rho [m]'); ylabel('z [m]');
407
408 % Convergence
409 subplot(2,3,6);
410 if ~isempty(err_hist)
411     semilogy(1:length(err_hist), err_hist*100, 'o-', 'LineWidth', 2);
412     hold on;
413     yline(1, 'r--', 'Target 1%', 'LineWidth', 2);
414     grid on;
415     xlabel('Number of Terms');
416     ylabel('Relative RMS Error (%)');
417     title('Convergence History');
418     legend('Error', 'Target');
419 end
420
421 saveas(fig1, sprintf('%s_results.png', rotor_type));
422
423 % 2. Coefficient Analysis
424 if length(k_list) > 1
425     fig2 = figure('Position', [100, 100, 1000, 400]);
426
427     subplot(1,2,1);
428     stem(1:length(C_list), abs(C_list), 'filled', 'LineWidth', 2);
429     set(gca, 'YScale', 'log');
430     grid on;
431     title('Coefficient Magnitudes');
432     xlabel('Term Index'); ylabel('|C(n)|');
433
434     subplot(1,2,2);
435     scatter(k_list, abs(C_list), 50, type_list, 'filled');
436     set(gca, 'XScale', 'log', 'YScale', 'log');
437     colorbar; grid on;
438     title('Coefficients vs Wave Number');
439     xlabel('k_n [1/m]'); ylabel('|C(n)|');
440
441     saveas(fig2, sprintf('%s_coefficients.png', rotor_type));
442 end
443
444 fprintf('Plots saved.\n');
445 end

```

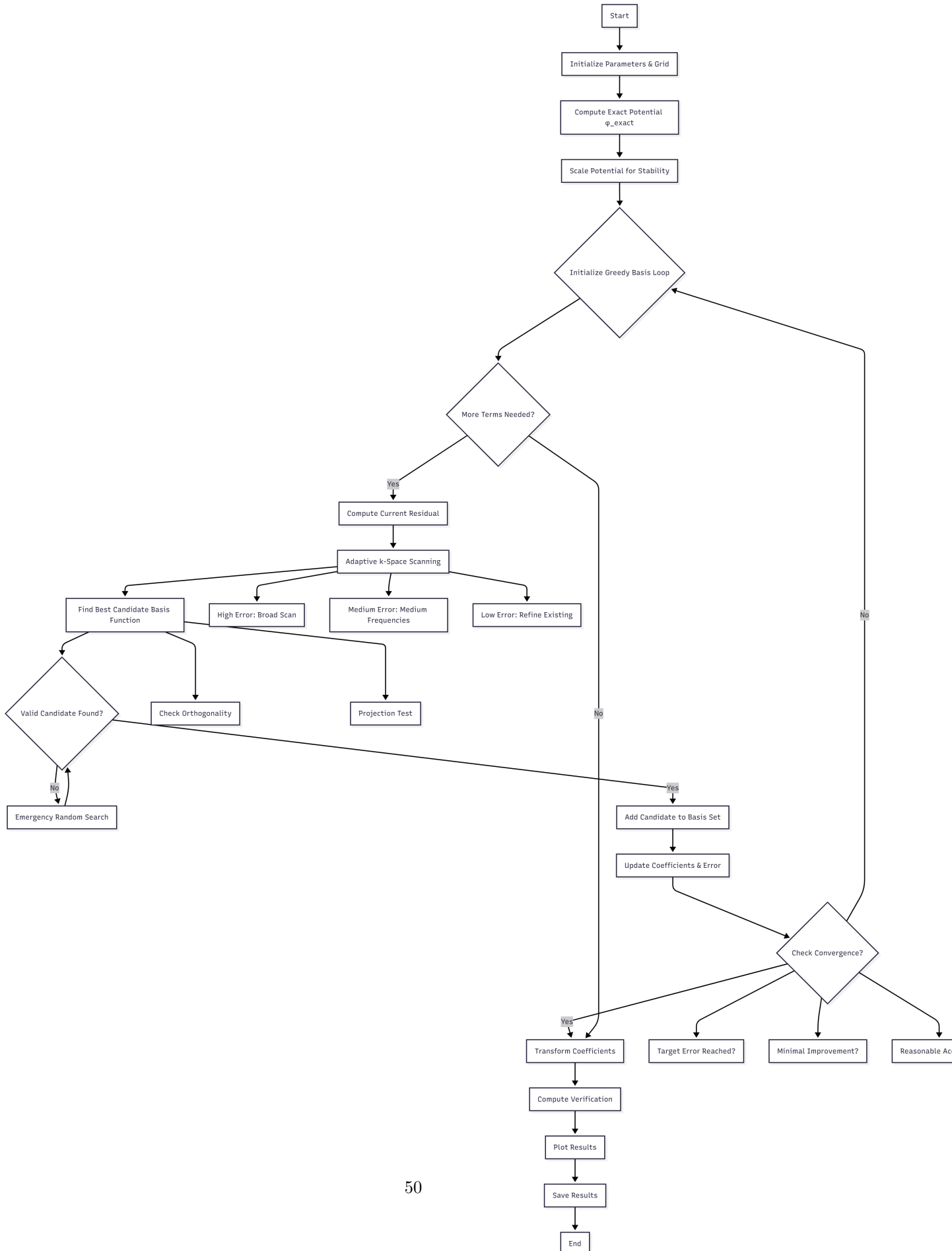
Listing 1: MATLAB code for Orthogonal Greedy Algorithm

Here are the coefficients given by the code.

Table 5: External Rotor (Region IV) Results

Index	k_n [1/m]	Bessel Type	$C(n)$
1	35.631940	Y_P	-5.58428
2	2.745342	J_P	1.59093e+12
3	545.550537	J_P	319828
4	1043.834705	J_P	-1.22532e+06
5	1716.148654	J_P	-1.12535e+06
6	179.912458	Y_P	-182550
7	555.658639	Y_P	1.26226e+06
8	2317.891437	Y_P	355574
9	2907.275370	J_P	-73867.5
10	1620.534842	J_P	-348568
11	3497.505992	Y_P	-202987
12	4169.559779	Y_P	-189943
13	4848.017806	Y_P	55642.5
14	2154.020186	J_P	-573913
15	2742.705678	Y_P	-678136
16	3497.505992	J_P	901420
17	5000.000000	J_P	155588
18	4321.292688	J_P	-527123
19	337.994550	Y_P	1.49258e+06
20	1038.905751	Y_P	-957105
21	5000.000000	Y_P	-76093.6
22	355.144121	J_P	705228
23	4693.732567	J_P	682303
24	1352.479865	J_P	1.27153e+06
25	125.770318	J_P	4.07008e+06
26	3849.305527	J_P	-735949
27	4508.853619	Y_P	-199547
28	782.583181	Y_P	1.22251e+06
29	1349.545939	Y_P	120742
30	85.078681	Y_P	3138.08
31	3082.755463	Y_P	921481
32	3845.285812	Y_P	2740.81
33	782.081824	J_P	-947800
34	1994.854573	Y_P	-829453
35	4861.932101	J_P	595308
36	51.264204	J_P	-5.47123e+07
37	228.063312	J_P	-1.70299e+06

Final RMS error: 0.815700%



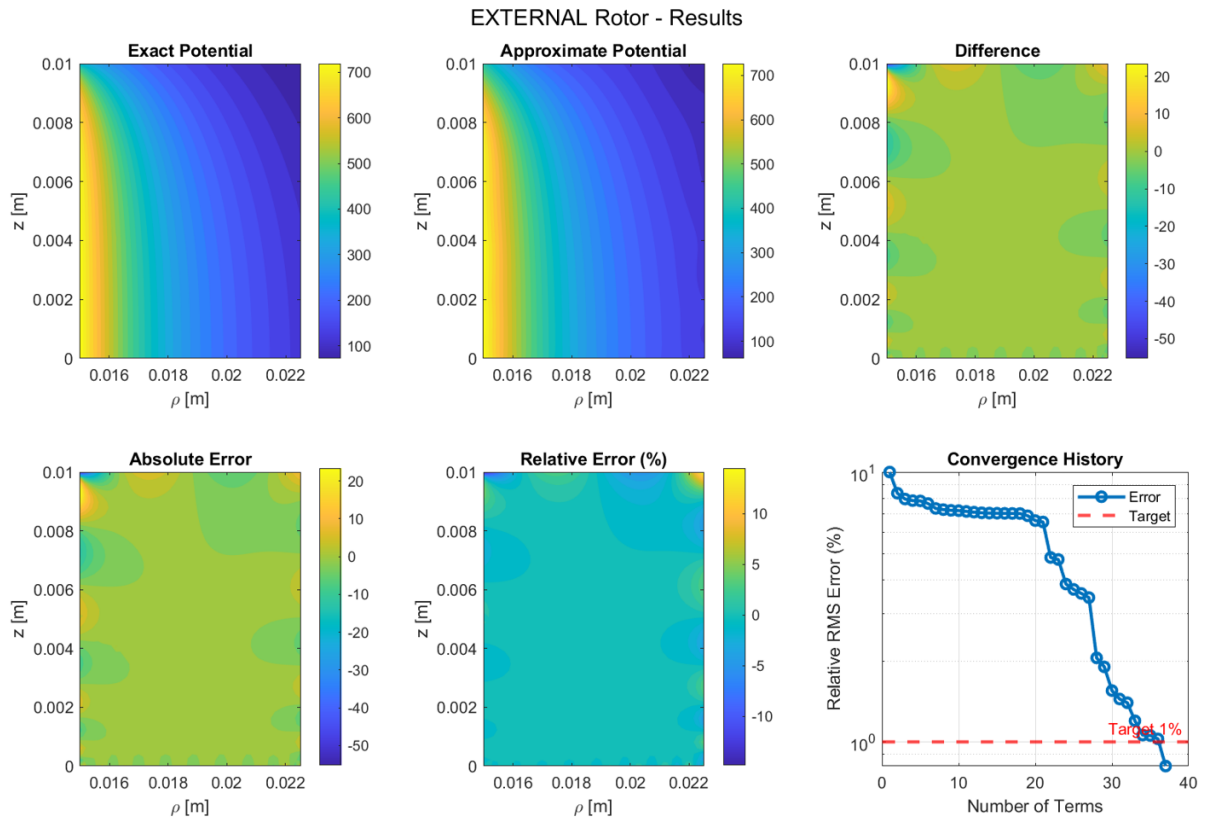


Figure 32: Field plot and convergence history

A4 Coefficients of Magnetic Components in the Air and Plate Region

To simplify calculations, the following variables are introduced:

$$k^2 = \xi^2 + \zeta^2, \quad \gamma^2 = \xi^2 + \zeta^2 + i\mu_0\sigma(\omega_e - v_x\xi) \quad (169)$$

$$\tilde{B}_x^s = \tilde{B}_x^s(\xi, y = -h_r, \zeta), \quad \tilde{B}_y^s = \tilde{B}_y^s(\xi, y = -h_r, \zeta), \quad \tilde{B}_z^s = \tilde{B}_z^s(\xi, y = -h_r, \zeta) \quad (170)$$

$$S_H = e^{kh_r}, \quad T_H = e^{-kh_r} \quad (171)$$

$$S_D = e^{kd_p}, \quad T_D = e^{-kd_p} \quad (172)$$

$$U = vS_H, \quad V = \nu T_D T_H \quad (173)$$

$$D = 2k \sinh(kd_p) \quad (174)$$

The coefficients are

$$\alpha_x = \frac{1}{T_H D} \left[S_D(-\tilde{B}_z^s + i\mu_0\zeta U) - i\mu_0\zeta V \right] \quad (175)$$

$$\beta_x = \frac{1}{S_H D} \left[T_D(-\tilde{B}_z^s + i\mu_0\zeta U) - i\mu_0\zeta V \right] \quad (176)$$

$$\alpha_y = \beta_y = 0 \quad (177)$$

$$\alpha_z = \frac{1}{T_H D} \left[S_D(\tilde{B}_x^s - i\mu_0\xi U) + i\mu_0\xi V \right] \quad (178)$$

$$\beta_z = \frac{1}{S_H D} \left[T_D(\tilde{B}_x^s - i\mu_0\xi U) + i\mu_0\xi V \right] \quad (179)$$

$$v = -\frac{T_H}{2\mu_0 k^2} \left[k\tilde{B}_y^s + i\zeta\tilde{B}_z^s + i\xi\tilde{B}_x^s \right] \quad (180)$$

$$\nu = \frac{S_H}{2\mu_0 k^2} \left[-k\tilde{B}_y^s + i\zeta\tilde{B}_z^s + i\xi\tilde{B}_x^s \right] \quad (181)$$